UNIVERSITYOF BIRMINGHAM

University of Birmingham Research at Birmingham

TESS Hunt for Young and Maturing Exoplanets (THYME). X. A Two-planet System in the 210 Myr MELANGE-5 Association

Thao, Pa Chia; Mann, Andrew W.; Barber, Madyson G.; Kraus, Adam L.; Tofflemire, Benjamin M.; Bush, Jonathan L.; Wood, Mackenna L.; Collins, Karen A.; Vanderburg, Andrew; Quinn, Samuel N.; Zhou, George; Newton, Elisabeth R.; Ziegler, Carl; Law, Nicholas; Barkaoui, Khalid; Pozuelos, Francisco J.; Timmermans, Mathilde; Gillon, Michaël; Jehin, Emmanuël; Schwarz, Richard P.

[Link to publication on Research at Birmingham portal](#)

TESS Hunt for Young and Maturing Exoplanets (THYME). X. A Two-planet System in the 210 Myr MELANGE-5 Association

Pa Chia Thao[1,23,24], Andrew W. Mann[1], Madyson G. Barber[1,25], Adam L. Kraus[2], Benjamin M. Tofflemire[2,26], Jonathan L. Bush[1], Mackenna L. Wood[1,3], Karen A. Collins[4], Andrew Vanderburg[3], Samuel N. Quinn[4], George Zhou[5], Elisabeth R. Newton[6], Carl Ziegler[7], Nicholas Law[1], Khalid Barkaoui[8,9,10], Francisco J. Pozuelos[8,11], Mathilde Timmermans[8], Michaël Gillon[8], Emmanuël Jehin[12], Richard P. Schwarz[4], Tianjun Gan[13], Avi Shporer[3], Keith Horne[14], Ramotholo Sefako[15], Olga Suarez[16], Djamel Mekarnia[16], Tristan Guillot[16], Lyu Abe[16], Amaury H. M. J. Triaud[17], Don J. Radford[18], Ana Isabel Lopez Murillo[1], George R. Ricker[3], Joshua N. Winn[19], Jon M. Jenkins[20], Luke G. Bouma[19], Michael Fausnaugh[3,21], Natalia M. Guerrero[22], and Michelle Kunimoto[3,27]

[1] Department of Physics and Astronomy, The University of North Carolina at Chapel Hill, Chapel Hill, NC 27599, USA; pachia@live.unc.edu
[2] Department of Astronomy, The University of Texas at Austin, Austin, TX 78712, USA
[3] Department of Physics and Kavli Institute for Astrophysics and Space Research, Massachusetts Institute of Technology, Cambridge, MA 02139, USA
[4] Center for Astrophysics | Harvard & Smithsonian, 60 Garden Street, Cambridge, MA 02138, USA
[5] Centre for Astrophysics, University of Southern Queensland, West Street, Toowoomba, QLD 4350, Australia
[6] Department of Physics and Astronomy, Dartmouth College, Hanover, NH 03755, USA
[7] Department of Physics, Engineering and Astronomy, Stephen F. Austin State University, 1936 North Street, Nacogdoches, TX 75962, USA
[8] Astrobiology Research Unit, Université de Liège, 19C Allée du 6 Août, 4000 Liège, Belgium
[9] Department of Earth, Atmospheric and Planetary Science, Massachusetts Institute of Technology, 77 Massachusetts Avenue, Cambridge, MA 02139, USA
[10] Instituto de Astrofísica de Canarias (IAC), Calle Vía Láctea s/n, 38200, La Laguna, Tenerife, Spain
[11] Instituto de Astrofísica de Andalucía (IAA-CSIC), Glorieta de la Astronomía s/n, 18008 Granada, Spain
[12] Space Sciences, Technologies and Astrophysics Research (STAR) Institute, Université de Liège, Allée du 6 Août 19C, B-4000 Liège, Belgium
[13] Department of Astronomy, Tsinghua University, Beijing 100084, People's Republic of China
[14] SUPA Physics and Astronomy, University of St. Andrews, Fife, KY16 9SS Scotland, UK
[15] South African Astronomical Observatory, P.O. Box 9, Observatory, Cape Town 7935, South Africa
[16] Université Côte d'Azur, Observatoire de la Côte d'Azur, CNRS, Laboratoire Lagrange, Bd de l'Observatoire, CS 34229, 06304 Nice cedex 4, France
[17] School of Physics & Astronomy, University of Birmingham, Edgbaston, Birmingham, B15 2TT, UK
[18] Brierfield Observatory, New South Wales, Australia
[19] Department of Astrophysical Sciences, Princeton University, 4 Ivy Lane, Princeton, NJ 08544, USA
[20] NASA Ames Research Center, Moffett Field, CA 94035, USA
[21] Department of Physics & Astronomy, Texas Tech University, Lubbock, TX 79410-1051, USA
[22] Department of Astronomy, University of Florida, Gainesville, FL 32811, USA

Abstract

Young (<500 Myr) planets are critical to studying how planets form and evolve. Among these young planetary systems, multiplanet configurations are particularly useful, as they provide a means to control for variables within a system. Here, we report the discovery and characterization of a young planetary system, TOI-1224. We show that the planet host resides within a young population we denote as MELANGE-5. By employing a range of age-dating methods—isochrone fitting, lithium abundance analysis, gyrochronology, and Gaia excess variability—we estimate the age of MELANGE-5 to be 210 ± 27 Myr. MELANGE-5 is situated in close proximity to previously identified younger (80–110 Myr) associations, Crius 221 and Theia 424/Volans-Carina, motivating further work to map out the group boundaries. In addition to a planet candidate detected by the TESS pipeline and alerted as a TESS object of interest, TOI-1224 b, we identify a second planet, TOI-1224 c, using custom search tools optimized for young stars (Notch and LOCoR). We find that the planets are $2.10 \pm 0.09\ R_\oplus$ and $2.88 \pm 0.10\ R_\oplus$ and orbit their host star every 4.18 and 17.95 days, respectively. With their bright ($K = 9.1$ mag), small ($R_* = 0.44\ R_\odot$), and cool ($T_{\rm eff} = 3326$ K) host star, these planets represent excellent candidates for atmospheric characterization with JWST.

Unified Astronomy Thesaurus concepts: Exoplanet astronomy (486); Transit photometry (1709); Stellar ages (1581); Young star clusters (1833); Stellar activity (1580); Transit timing variation method (1710)

Supporting material: machine-readable table

---

[23] NSF Graduate Research Fellow.
[24] Jack Kent Cooke Foundation Graduate Scholar.
[25] NSF Graduate Research Fellow.
[26] 51 Pegasi b Fellow.
[27] Juan Carlos Torres Postdoctoral Fellow.

1. Introduction

Young planets (<0.5 Gyr) offer a powerful means to study the formation and evolution of planetary systems. Similar to our own solar system, exoplanets are expected to go through rapid evolution in the first few hundred million yr after formation (Alexander et al. 2001; Morbidelli et al. 2012). Throughout this early stage, planets are likely to undergo changes in their orbital (Chatterjee et al. 2008), structural (Owen 2020), and atmospheric (Öberg et al. 2011; Booth et al. 2017; Booth & Ilee 2019)

properties. Discovery and characterization of planets in this age range offers a unique window into the dynamic processes that shape planetary systems.

The K2 and Transiting Exoplanet Survey Satellite (TESS) missions have enabled the discovery of transiting planets in young associations ranging from 10 Myr (e.g., Mann et al. 2016b; David et al. 2016) to 700 Myr (e.g., Obermeier et al. 2016; Rizzuto et al. 2017; Curtis et al. 2018). Some similarly young planets in coeval populations have even been discovered in the Kepler prime field (Bouma et al. 2021, 2022; Barber et al. 2022). The statistics of these systems have provided early evidence that young planets are larger than their older counterparts (Mann et al. 2017; Fernandes et al. 2022). Follow-up of such systems has provided evidence that the orbits of some young, close-in planets are aligned with the equators of their host stars (Zhou et al. 2020; Johnson et al. 2022) and has provided an early look at the atmospheres of young planetary systems (e.g., Libby-Roberts et al. 2020; Thao et al. 2020, 2023).

Despite significant advances in recent years, the population of young transiting planets is still relatively small, falling short of the comprehensive data set required for robust statistical analysis. The age distribution of known young planets is also heavily biased towards <150 Myr and ≃700 Myr (Newton et al. 2022). This is primarily because there are numerous nearby young groups and OB associations covering the youngest ages (e.g., Taurus-Auriga and Sco-Cen; David et al. 2019; Rizzuto et al. 2020) and several large clusters sampling the higher end (Hyades and Praesepe; Mann et al. 2017; Vanderburg et al. 2018). The sample of 200–400 Myr planets is drawn primarily from newly identified associations (e.g., Hedges et al. 2021; Tofflemire et al. 2021).

Here, we report the discovery of a new ≃200 Myr association, Membership and Evolution by Leveraging Adjacent Neighbors in a Genuine Ensemble (MELANGE-5), along with a two-planet transiting system orbiting one of its member stars, namely, TOI-1224 or TIC 299798795. In Section 2, we present comprehensive details of all follow-up observations of TOI-1224 and its parent population. In Section 3, we detail the observations and analysis of MELANGE-5 association members. In Section 4, we investigate the properties of the MELANGE-5 association, including its estimated age. In Section 5, we delve into the specific properties of the planet-hosting star, and in Section 6, we present a detailed analysis of the properties of the two planets in the system. Finally, in Section 7, we provide a concise summary of our work and highlight the broader implications of these findings. We showcase their contribution to the expanding catalog of multiplanet systems and emphasize the significance of these newly discovered planets as prime candidates for future atmospheric characterization studies.

2. Observation of TOI-1224 and Data Reduction

2.1. TESS

TOI-1224 (TIC 299798795) was first observed by TESS (Ricker 2014) in Sector 1, which took place from 2018 July 25 to August 22. Subsequently, the target was reobserved by TESS during Sector 13 (2019 June 19 to July 17), Sector 27 (2020 July 5 to July 30), Sector 28 (2020 July 31 to August 25), Sector 39 (2021 May 27 to June 24), Sector 66 (2023 June 2 to July 1), Sector 67 (2023 July 1 to July 29), and Sector 68 (2023 July 29 to August 25). For the Sector 1 and 13 data, the target was preselected for 120 s cadence for two guest investigator programs: G011180 (PI: C. Dressing) and

G011238 (PI: S. Lepine). In the case of the latter six sectors (Sectors 27, 28, 39, 66, 67, and 68), the target was preselected for 20 s cadence as part of four guest investigator programs: G03174 (PI: W. Howard), G03278 (PI: A. Mayo), G03202 (PI: R. Paudel), and G05064 (PI: W. Howard). The short-cadence observations were motivated by the star's brightness, the presence of flares, and the previous detection of a planet candidate (Moranta et al. 2022).

We have found that the presearch data conditioning simple aperture photometry (Smith et al. 2012; Stumpe et al. 2012, 2014) TESS light curve produced by the Science Process Operations Center (SPOC; Jenkins et al. 2016) struggles on young stars with high-amplitude stellar variability. Despite these difficulties, both planets were successfully identified by SPOC, as detailed in Section 6.1. Instead, we extracted the photometry with a custom pipeline following Vanderburg et al. (2019). This started with the simple aperture photometry curves (Twicken et al. 2010), which we fit with a linear model consisting of a 0.3 day basis spline, the mean and standard deviation of the spacecraft quaternion time series, seven cotrending vectors from the SPOC data conditioning, and a high-pass-filtered time series from the SPOC background aperture. Errors for each sector of data were calculated using the standard deviation of the detrended and normalized out-of-transit data. This yielded errors of ∼0.002 and 0.005 for the 120 and 20 s cadence data.

Since 120 and 20 s cadence are both available for Sectors 27, 28, 39, 66, 67, and 68, we elected to utilize only the 20 s data for these sectors, as the shorter cadence yields the best precision even when the data are binned back to a slower cadence (Huber et al. 2022).

Prominent flares were observed in the custom-extracted light curves (also see Howard et al. 2019; Günther et al. 2020). To mitigate their impact, we used stella,[28] a convolutional neural network trained for flare detection in the TESS short-cadence data (Feinstein et al. 2020). Utilizing the 10 models established in Feinstein et al. (2020), we obtained an average flare prediction for each data point. Any data points with a flare probability of >80% were excluded from the analysis. This led to the removal of 4.47%, 3.27%, 0.62%, 0.26%, 0.22%, 0.43%, 0.45%, and 0.15% of the data for Sectors 1, 13, 27, 28, 39, 66, 67, and 68, respectively. The variability in flare removal can be attributed to strong variations in the levels of stellar activity and cadence differences (which impacts sensitivity to flares) between different sectors.

2.2. Antarctica Search for Transiting ExoPlanets Photometry

The Antarctica Search for Transiting ExoPlanets (ASTEP) program on the East Antarctic plateau (Guillot et al. 2015; Mékarnia et al. 2016) observed three transits of planet c on the following dates: 2022 July 4, 2022 July 22, and 2022 September 14 (UT). The observations on September 14 did not yield a detectable transit signal, likely attributed to a potential transit-timing variation (TTV; Section 6.3); as a result, these data were excluded from the subsequent analysis. However, the remaining two observations successfully captured the transit signal. The error bars for both data sets had to be adjusted to ensure that the standard deviation in the normalized out-of-transit flux was equal to the median flux error. Scaling was applied to the data sets, with a factor of 4 for the 2022 July 4 data set and a factor of 2 for the 2022 July 22 data set.

---

[28] ⌂ https://github.com/afeinstein20/stella

Telescope	Filter	Exp. Time (s)	Planet	Start Date (UT)
TESS Sector 1	TESS	120	b, c	2018 Jul 25
TESS Sector 13	TESS	120	b, c	2019 Jun 19
TESS Sector 27	TESS	20	b, c	2020 Jul 4
TESS Sector 28	TESS	20	b, c	2020 Jul 30
TESS Sector 39	TESS	20	b, c	2021 May 26
TESS Sector 66	TESS	20	b,c	2023 Jun 2
TESS Sector 67	TESS	20	b,c	2023 Jul 1
TESS Sector 68	TESS	20	b,c	2023 Jul 29
ASTEP[a]	R	100	c	2022 Jul 4
ASTEP	R	100	c	2022 Jul 22
LCO-SAAO	g_p	205	b	2020 Aug 14
LCO-SSO	g_p	240	c	2022 Dec 13
LCO-SSO	z_s	55	b	2020 Aug 5
LCO-SAAO	z_s	65	b	2020 Aug 14
LCO-SAAO	z_s	65	b	2020 Sep 3
LCO-SSO	z_s	65	c	2022 Oct 10
TRAPPIST-South[a]	z	25	b	2020 Dec 8
TRAPPIST-South	z	35	b	2021 Jan 2

Note.
[a] Only a partial transit was observed.

The 0.4 m telescope is equipped with two back-illuminated cameras operating in the $B + V$ bands similar to Gaia B (FLI Kepler KL400 sCMOS camera, 2048×2048 pixels) and in a red band close to the Gaia R band (Andor iKon-L 936 CCD camera, 2048×2048 pixels). These cameras have an image scale of $1{.}''05$ and $1{.}''30\,\mathrm{pixel}^{-1}$, respectively, resulting in $36 \times 36\,\mathrm{arcmin}^2$ and $44 \times 44\,\mathrm{arcmin}^2$ corrected fields of view (see Schmider et al. 2022 for further details). The fast full-frame reading rate of the sCMOS sensor in the blue channel is used to guide the telescope mount at a typical rate of 0.5 Hz, and these short-exposure images are stacked to generate typical exposure times of about 1 minute. However, due to hardware signal transmission issues during the winter campaign of 2022, the blue camera could only be used during half of the season, thus leaving the red channel Andor camera as the only scientific detector for the rest of the austral winter. Exposure times and observation dates are given in Table 1.

Due to the low data transmission rate at the Concordia Station, the data are processed on site using an automated IDL-based pipeline described in Abe et al. (2013). The calibrated light curve is reported via email, and the raw light curves of about 1000 stars are transferred to Europe on a server in Rome, Italy, and then available for deeper analysis. These data files contain each star's flux computed through 10 fixed circular aperture radii so that optimal light curves can be extracted.

2.3. Brierfield Observatory Photometry

We observed two transits of planet b on 2019 October 1 and 2020 August 1 taken in the Johnson I filter using a 0.36 m PlaneWave CDK14 telescope at the Brierfield Observatory, located in New South Wales, Australia. The imaging system employed a Moravian 16803 camera with a pixel scale of $1{.}''45\,\mathrm{pixel}^{-1}$. Unfortunately, the obtained light curves did not

possess the precision required for a clear detection of the transit. As a result, we decided not to include them in our transit fits.

2.4. Las Cumbres Observatory Global Telescope Photometry

We observed a total of six transits with 1 m telescopes in the Las Cumbres Observatory Global Telescope (LCOGT) network (Brown et al. 2013). We used the TESS `Transit Finder` tool, which is a customized version of the Tapir software package (Jensen 2013), to schedule the observations. These were all observed with Sinistro cameras, with a pixel scale of $0{.}''389\,\mathrm{pixel}^{-1}$. Two transits were observed using the Sloan Digital Sky Survey (SDSS) g' filter, one transit for planet b (2020 August 14) and one for planet c (2021 December 13), and four transits were observed using the SDSS z_s filter, three transits for planet b (2020 August 5, 2020 June 14, and 2020 September 3) and one for planet c (2022 October 2). For both observations of planet c in the SDSS g' and SDSS z' filters, error scaling was implemented with a factor of 2. This adjustment ensured that the standard deviation in the normalized out-of-transit data equaled the median flux error value.

The images were initially calibrated by the standard LCOGT `BANZAI` pipeline (McCully et al. 2018). We then performed aperture photometry on all data sets using the `AstroImageJ` package (Collins et al. 2017). The aperture varied based on the seeing conditions at the observatory, but we generally used a 6–10 pixel radius circular aperture for the source and an annulus with a 15–20 pixel inner radius and a 25–30 pixel outer radius for the sky background. For all observations, we centered the apertures on the source and weighted pixels within the aperture equally. All target star photometric apertures excluded flux from all known nearby Gaia DR3 stars. Since the event was detected on the source, the usual check of nearby sources for evidence of an eclipsing binary was not necessary. Light curves of nearby sources are available with the extracted light curves and further details on the follow-up at ExoFOP-TESS[29] (ExoFOP 2019). Exposure times and observation dates are given in Table 1.

2.5. TRAPPIST-South Photometry

We observed two transits of planet b with TRAPPIST-South (Gillon et al. 2011; Jehin et al. 2011), a 0.6 m Ritchey–Chrétien robotic telescope at La Silla Observatory in Chile. The TRAPPIST-South telescope is equipped with a $2K \times 2K$ back-illuminated CCD camera with a pixel scale of 0.65 pixel^{-1}, resulting in a field of view of $22' \times 22'$. We took both transits with a Sloan z' filter.

We used the TESS `Transit Finder` tool to schedule the observations. For data reduction and extracting photometry, we used the `PROSE`[30] pipeline (Garcia et al. 2022). Exposure times and observation dates are given in Table 1.

2.6. SMARTS/CHIRON

We observed TOI-1224 during four nights (2020 November 13, 2021 August 1, 2023 February 15, and 2023 February 16) with the CHIRON spectrograph on the 1.5 m SMARTS telescope (Tokovinin et al. 2013). CHIRON is a high-resolution echelle spectrograph fed by an image slicer and a fiber bundle located at Cerro Tololo Inter-American Observatory, Chile. The

---

[29] https://exofop.ipac.caltech.edu/tess/target.php?id=360156606
[30] PROSE: https://github.com/lgrcia/prose.

Table 2
RV Measurements of TOI-1224

JD-2450000	v (km s^{-1})	σ_v (km s^{-1})	Instrument
9166.6767	14.0	11.3	CHIRON
9427.9242	12.41	0.60	CHIRON
9990.5292	11.51	0.49	CHIRON
9991.5496	12.03	0.66	CHIRON

observations were obtained in the low-resolution fiber mode, yielding a spectral resolution of $R \sim 28{,}000$. We used the official CHIRON pipeline to extract the spectra as per Paredes et al. (2021). Radial velocities (RVs) are derived from a least-squares deconvolution against a nonrotating synthetic template generated from the ATLAS9 atmospheric library (Castelli & Kurucz 2004). We list the velocities in Table 2. In addition, we measure a rotational broadening of $v \sin i_\star = 22.1 \pm 1.2$ km s^{-1} from the line broadening profile of the highest signal-to-noise ratio (SNR) spectrum.

2.7. Speckle Imaging

We observed TOI-1224 on 2020 February 10 from the 4.1 m Southern Astrophysical Research (SOAR) telescope with speckle interferometry in the I-band (Tokovinin et al. 2018). We took these observations following the general observing strategy for TESS targets as described in Ziegler et al. (2020). This yielded an estimated contrast limit of $\Delta I = 6.2$ at $1''$ (Figure 1). We detected no companions.

3. Observations and Analysis of MELANGE-5 Candidate Members

Our motivation for observing the candidate members of MELANGE-5 was threefold: to confirm the existence of the association, to ascertain that it constitutes a single-aged population, and to precisely measure its age. We also sought to explore the relationship between this group and nearby ones identified in Moranta et al. (2022).

3.1. Target Selection and Identification of MELANGE-5

We initially searched for a candidate association around TOI-1224 using the open-source code `Comove`,[31] which is described in detail in Tofflemire et al. (2021). To briefly summarize, `Comove` utilizes the astrometric data from Gaia Data Release 3 (DR3; Lindegren et al. 2021) to identify stars that exhibit potential comoving characteristics within a specified spatial and kinematic range. It estimates the 3D distance and expected tangential velocity ($V_{\rm off}$) of all stars within the defined radius assuming a UVW matching TOI-1224 and utilizing RV data from Gaia DR3 and archival sources.

We initially selected stars with a tangential velocity difference of <5 km s^{-1} and a position <50 pc of TOI-1224. The resulting target list was heavily contaminated by unassociated stars, as evident from a large spread in the color–magnitude diagram (CMD) and RVs, as well as a significant population of cool white dwarfs. As we discuss further in Section 4.3, a significant portion of the contamination comes from a nearby younger population (which could bias our
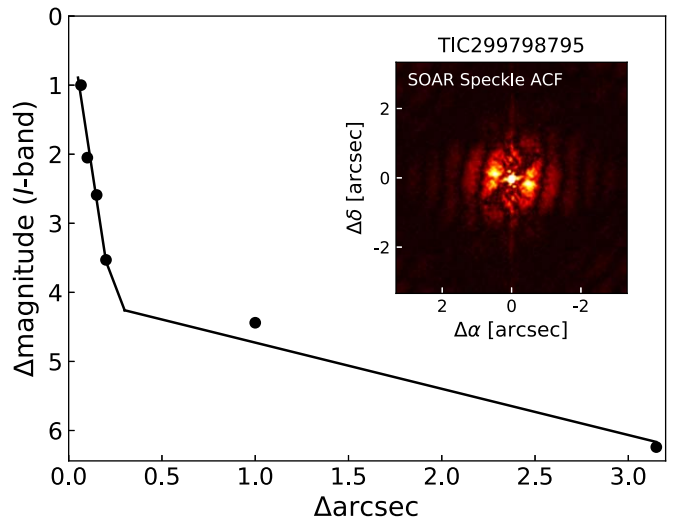
Figure 1. Detection limits from the speckle images of TOI-1224. The subpanel in the top right shows the narrowband 8320 Å reconstructed image.

age estimates). Thus, we opted for a tighter cut of 3 km s^{-1} and 35 pc. This yielded a list of 159 stars.

The resulting list formed a relatively tight CMD (Figure 2) consistent with a single-aged main-sequence population and a handful of outliers (a mix of nonmembers and poorer photometry/astrometry). Selected stars also cluster around the expected central RV (again with some clear outliers; Figure 2). Since RV and CMD information were not used to select members, these are compelling pieces of evidence that the grouping represents a real association. We refer to this association as MELANGE-5, following the scheme from earlier papers (Tofflemire et al. 2021).

The selection above is overinclusive, in that there are obvious outliers in kinematic, spatial, and CMD space. Additional down-selections, such as enforcing an RV cut, would likely yield a cleaner list. However, we have adopted a more inclusive list to start and perform additional cuts as needed to better determine the age in Section 4.1.5.

3.2. Spectroscopy

3.2.1. LCO Network of Robotic Echelle Spectrographs

We obtained high-resolution ($R \simeq 53{,}000$) optical (3800–8600 Å) spectra of candidate association members using the LCO Network of Robotic Echelle Spectrographs (NRES; Siverd et al. 2018). We prioritized targets with $G < 9$ to ensure SNR > 20 around the 6707 Å lithium line. In total, we obtained spectra for five targets this way.

All NRES data were reduced and wavelength calibrated using the BANZAI-NRES pipeline[32] (McCully et al. 2022).

3.2.2. Archival High Accuracy Radial velocity Planet Searcher Spectra

We downloaded spectra from the ESO science archive taken with the High Accuracy Radial velocity Planet Searcher (HARPS; Mayor et al. 2003) fiber-fed echelle spectrograph at the ESO La Silla 3.6 m telescope. HARPS spectra cover a spectral range of 3780–6910 Å at high resolution

---

[31] https://github.com/adamkraus/Comove

[32] https://github.com/LCOGT/banzai-nres
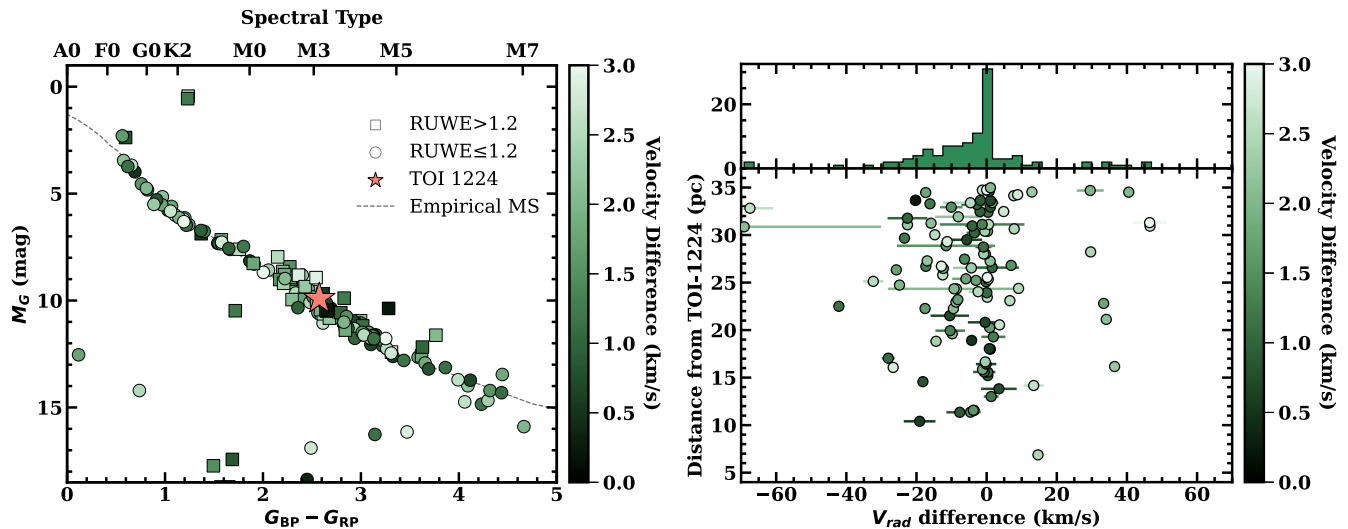
Figure 2. Left: CMD of sources within 35 pc and 3 km s^{-1} of TOI-1224. Points are color-coded by their velocity difference, and TOI-1224 is denoted as a pink star. Targets with a high RUWE (more likely to be binaries) are denoted as squares. RV data are extracted from Gaia DR3 and archival sources. Right: RVs of candidate members of MELANGE-5 compared to the value predicted assuming they have identical *UVW* to TOI-1224. RV data are extracted from Gaia DR3 and archival sources. The excess of points around zero is far above what is possible by chance and is far narrower than the velocity distribution of all solar neighborhood stars. Stars closer to zero RV difference are also statistically closer in tangential velocity. The excess of sources below (but near) zero may be due to uncertainties in TOI-1224's velocity, with TOI-1224 landing slightly off-center of the association, or coincident alignment with other groups (see Section 4) or Galactic motions.
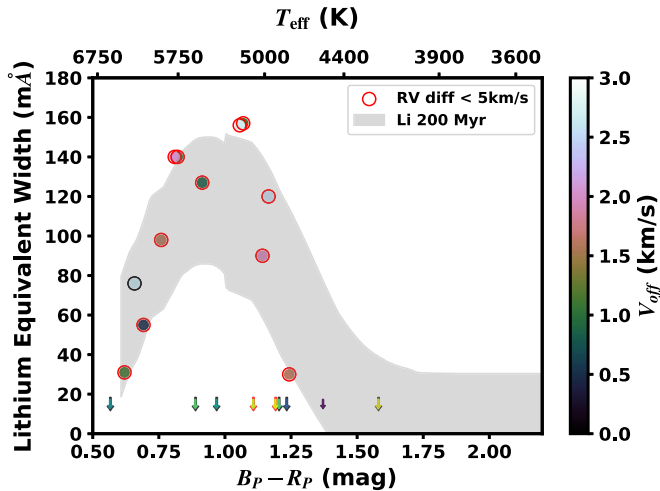
Figure 3. Lithium EWs of candidate members of MELANGE-5 as a function of Gaia color. The top axis shows the approximate T_{eff} for reference. Points are color-coded based on their RV. Non- or weak detections are shown as arrows. Targets with RVs within 5 km s^{-1} of the predicted value are outlined in red. The predicted 200 Myr sequence from `EAGLES` is shaded.

($R \simeq 115,000$). Archival spectra were taken as early as 2014 and as late as 2020. We required an SNR of at least 30 around the 6707 Å Li line. In the case of multiple spectra for the same target, we use the one with the highest SNR. In total, we retrieved spectra for 15 candidate members of MELANGE-5.

The ESO archive provided HARPS data reduced with the standard online HARPS data reduction pipeline.

3.2.3. Li Equivalent Widths

Lithium is destroyed in the interiors of stars. Mixing can therefore deplete lithium levels in the photosphere, creating a relation between age and the measured lithium abundance. For fully convective stars, total Li depletion is rapid. For Sun-like stars, Li depletion depends on the mixing timescale and the depth of the convective regions. Additional effects, like rotation, complicate this relation and add significant scatter even for single-aged populations (Somers & Pinsonneault 2015). Still, the lithium levels in a range of stars within a cluster can provide a useful constraint on the association's age.

We measured the equivalent width (EW) of the 6708 Å Li line from the HARPS and NRES spectra (Section 2). We first placed the reduced spectra into the star's rest frame by cross-correlating against a matching PHOENIX model (Husser et al. 2013). We then performed a least-squares fit to the region around the Li line (6706–6710 Å) assuming a Gaussian. We removed other spectral lines in the region using a 5σ iterative clipping. We used the estimate of the continuum level and line width from the Gaussian to calculate the EW.

For nearly all stars, the spectral resolution was sufficient to separate out the nearby iron line. For those with visible contamination, we fit a double Gaussian and subtracted the iron line model before computing the EW.

We estimated the uncertainties on our EWs using a Monte Carlo (MC) approach. Specifically, we perturbed the spectra, refit the line, then recomputed the EW 10,000 times and used the scatter in the resulting values as a proxy for the uncertainty. Comparison to EWs from Tofflemire et al. (2021), Barber et al. (2022), and Newton et al. (2022) suggest that these uncertainties are missing a systematic error term of $\simeq$10 mA, which we added in on top of the MC uncertainties. The same analysis (MC and comparison to existing measurements) indicated that we are insensitive to EWs below 20 mÅ; we set all nondetections to this limit.

We drew two additional lithium measurements from Torres et al. (2008). These EWs were estimated using similar high-resolution spectra, and comparison between their targets and those with NRES or HARPS data showed a negligible offset and comparable uncertainties. The results of our detailed abundance measurements are detailed in Table 3.
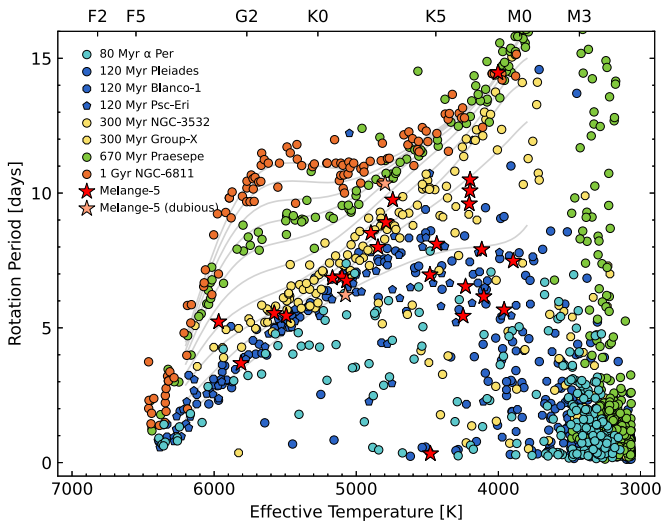
Figure 4. Rotation periods of MELANGE-5 compared to rotation periods of benchmark open clusters. MELANGE-5 members are represented by red stars, and the shade indicates the quality of the rotation, with darker red (0) representing a clearly observed rotation in the light curve and lighter red (1) representing a questionable period. MELANGE-5 falls above the 120 Myr clusters and slightly below the 300 Myr clusters. The gray lines are the "mean" empirical isochrones fitted by Bouma et al. (2023) with ascending time intervals of 100 Myr, 200 Myr, and so on. The astrophysical scatter about these mean lines sets the empirical precision limit for this age-dating method.

3.3. TESS Photometry

We extract TESS light curves for candidate association members using causal pixel models (Wang et al. 2016) run on the full-frame images. Specifically, we used the `unpopular` package[33] to build a model of systematics (Hattori et al. 2021). The details of the `unpopular` extraction used here are reported in Barber et al. (2022), Vowell et al. (2023), and Wood et al. (2023), each of which were applied to measuring rotation periods in young associations.

3.4. Rotation Periods

To ensure that we get high-quality rotation periods, we first removed those stars with $T > 15$ mag and/or a flux contamination ratio >1.5.

To estimate the rotation period of each target, we employed the Lomb–Scargle (LS; Horne & Baliunas 1986) algorithm using the fast implementation (Press & Rybicki 1989) in `astropy`. For each sector of TESS photometry, we searched over a period range of 0.1–15 days, adopting the peak in the LS periodogram as a candidate period. Across sectors, we selected the period corresponding to the highest LS power. To confirm these measurements, we phase-folded the single-quarter light curves to the candidate period and examined the signals' consistency across quarters. We performed an eye check in the style of Rampalli et al. (2021), labeling obvious rotations as Q0, questionable rotations as Q1, spurious detections as Q2, and nondetections as Q3.

We retained only Q0 and Q1 periods. In total, 87 stars passed this cut. The remainder is a mix of nonmembers and targets too faint for reliable extraction of the TESS light curve. A summary of each period and quality assessment can be found in Table 3.
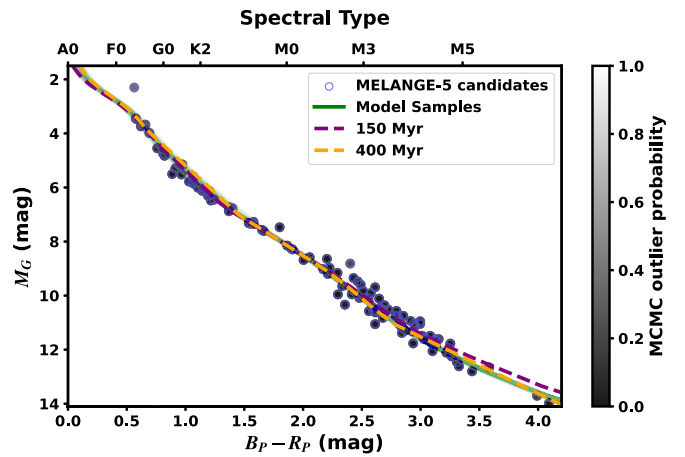
Figure 5. Example CMD of MELANGE-5 (black circles) fit using a mixture model. Each point is shaded by the probability of being part of the primary population (the single-star single-aged group). The green lines are 100 random draws from the Markov chain Monte Carlo (MCMC) posterior. For reference, we included 400 and 150 Myr isochrones.

4. Properties of the MELANGE-5 Association

4.1. Age

4.1.1. Lithium-based Age

We show the lithium EWs of potential members in Figure 3. We converted these measurements into an age estimate of the association using the `EAGLES`[34] software (Jeffries et al. 2023). `EAGLES` was calibrated using spectroscopy from the Gaia-ESO survey of clusters with well-established ages (e.g., Jackson et al. 2022; Randich et al. 2022).

The `EAGLES` code is not designed to work with non-members included, so we only included targets with RVs within $5 \, \mathrm{km \, s^{-1}}$ of the predicted value. This left 14 stars. `EAGLES` works in T_{eff}, so we converted the observed Gaia $B_P - R_P$ colors to T_{eff} using the Pecaut & Mamajek (2013) empirical tables.[35]

We ran `EAGLES` in "cluster" mode, including uncertainties on T_{eff} and lithium, which yielded an age of 177^{+45}_{-36} Myr. There are two stars in the sample with no detected lithium even though a detection would be expected at this age. Both stars land near the tangential velocity cutoff for selecting members (Section 3.1), suggesting they might not be members. Removing these two stars resulted in an age of 185 ± 35 Myr —an insignificant effect on the age and a small reduction on the upper uncertainty. Either age was consistent with all other determinations, although our isochrone fit rules out the lower end of both posteriors (<150 Myr).

4.1.2. Gyrochrone Age

We show the P_{rot}–color sequence for MELANGE-5 alongside younger benchmark open clusters in Figure 4. The rotation periods for these clusters are from α Per (Boyle & Bouma 2023), the Pleiades (Rebull et al. 2016), Blanco-1 (Gillen et al. 2020), Psc-Eri (Curtis et al. 2019b), NGC 3532 (Fritzewski et al. 2021), Group-X (Messina et al. 2022), Praesepe (Douglas et al. 2019), and NGC 6811 (Curtis et al. 2019a). To generate the plot, we

---

[33] ⛓ https://github.com/soichiro-hattori/unpopular

[34] ⛓ https://github.com/robdjeff/eagles

[35] https://www.pas.rochester.edu/~emamajek/EEM_dwarf_UBVIJHK_colors_Teff.txt

Table 3
MELANGE-5 Members

Gaia DR3	TIC	α J2016.0	δ J2016.0	RV (km s^{-1})	σ_{RV} (km s^{-1})	RV Source	EqW Li (mÅ)	σ_{EqWLi} (mÅ)	Li Source	P_{rot} (days)	Rotation Quality
4620009665047355520	299798795	37.19798	−80.8991	14.63	1.92	Gaia DR3	⋯	⋯	⋯	1.23	0.0
5194732707942826496	278290227	112.69671	−82.43623	32.04	0.31	Gaia DR3	⋯	⋯	⋯	6.74	1.0
4692269642240299776	52242947	19.93763	−68.71285	⋯	⋯	None	⋯	⋯	⋯	0.44	0.0
6357002092906608512	287148041	338.14076	−76.93951	−10.44	4.52	Gaia DR3	⋯	⋯	⋯	1.21	0.0
5765467482863792768	290492468	241.10938	−87.40711	5.19	3.81	Gaia DR3	⋯	⋯	⋯	1.51	3.0
6369133825033348224	271577579	319.40123	−74.56481	1.64	2.94	Gaia DR3	⋯	⋯	⋯	0.71	0.0
6387813329294043520	402066134	352.75559	−69.08691	3.95	0.14	Gaia DR3	30.0	11.5	HARPS	⋯	⋯
6387813336653800448	402066136	352.76417	−69.07728	3.73	0.13	Gaia DR3	98.0	14.9	NRES	5.22	0.0
6361384535800070144	1987797195	303.43602	−80.46513	⋯	⋯	None	⋯	⋯	⋯	3.92	0.0
5267405895350690304	300015239	107.18725	−70.49845	⋯	⋯	None	⋯	⋯	⋯	12.77	2.0
6369133829329588352	271577578	319.40049	−74.56729	7.54	2.12	Gaia DR3	⋯	⋯	⋯	⋯	⋯
5265069360124273536	141756992	91.45159	−73.95555	⋯	⋯	None	⋯	⋯	⋯	9.57	0.0
5771258644968448256	418720125	210.17054	−82.22629	16.57	5.08	Gaia DR3	⋯	⋯	⋯	0.47	0.0
4700296214561766144	358577029	38.53702	−63.38986	29.1	2.86	Gaia DR3	⋯	⋯	⋯	3.39	0.0
5267405964069463680	300015238	107.17669	−70.49661	4.97	1.17	Gaia DR3	⋯	⋯	⋯	⋯	⋯
5780799416601562496	426533052	244.59667	−76.56144	⋯	⋯	None	⋯	⋯	⋯	0.64	0.0
6416270751806848512	466680054	295.39885	−72.44675	4.6	0.14	Gaia DR3	157.0	17.85	NRES	6.74	0.0
4624764296923659648	140827419	75.25472	−77.09649	⋯	⋯	None	⋯	⋯	⋯	⋯	⋯
6420588087293438976	409883397	293.79044	−69.97636	3.22	0.13	Gaia DR3	140.0	17.0	HARPS	3.92	⋯
6421013254696711296	381982077	284.00151	−70.69675	2.72	3.18	Gaia DR3	⋯	⋯	⋯	0.26	1.0
5196110606467412864	323008198	125.97079	−81.97343	16.34	1.56	Gaia DR3	⋯	⋯	⋯	⋯	3.0
6396236859672379008	327669585	330.07931	−68.00669	−22.69	0.24	Gaia DR3	⋯	⋯	⋯	6.74	1.0
6418732764501078784	467939527	283.81072	−71.2518	40.2	0.82	Gaia DR3	⋯	⋯	⋯	7.2	1.0
6370853602954758272	404348184	321.36359	−73.18337	5.52	2.91	Gaia DR3	⋯	⋯	⋯	0.67	0.0
5482185145257567232	150188736	93.72865	−60.65534	25.0	0.57	Gaia DR3	⋯	⋯	⋯	9.38	0.0
5287064510419675776	348893965	105.90952	−61.57045	⋯	⋯	None	⋯	⋯	⋯	⋯	⋯
4757301941103536000	309790592	80.21079	−63.41597	−4.86	1.84	Gaia DR3	⋯	⋯	⋯	3.15	2.0
4616276930446765824	318612083	7.57222	−86.23213	14.21	0.21	Gaia DR3	⋯	⋯	⋯	6.85	0.0
5202659778759682048	453442366	151.93055	−77.81114	18.94	0.35	Gaia DR3	⋯	⋯	⋯	7.48	0.0
6356860393345181952	317057431	336.87475	−77.7182	⋯	⋯	None	⋯	⋯	⋯	⋯	⋯
4723828890132788992	207234477	49.53	−59.38435	3.93	1.7	Gaia DR3	⋯	⋯	⋯	⋯	3.0
6394241555306538240	237313246	343.79502	−63.1757	⋯	⋯	None	⋯	⋯	⋯	⋯	3.0
6356860393345181824	317057430	336.88045	−77.71833	4.61	0.13	Gaia DR3	55.0	12.75	HARPS	5.52	2.0
5194066717430657792	404875401	93.78974	−84.64923	⋯	⋯	None	⋯	⋯	⋯	0.59	0.0
6418406690583059712	467934114	282.22234	−72.5607	6.4	3.43	Gaia DR3	⋯	⋯	⋯	3.67	0.0
5270707831848146944	453099619	116.08608	−69.5106	13.19	0.16	Gaia DR3	⋯	⋯	⋯	2.34	2.0
6400051752705452544	410058419	321.05689	−67.5699	−7.58	4.21	Gaia DR3	⋯	⋯	⋯	0.58	0.0
5208911047821367296	278518946	120.64858	−79.24193	19.71	1.53	Gaia DR3	⋯	⋯	⋯	3.12	0.0
5223796927729858816	303166531	137.28797	−67.99446	⋯	⋯	None	⋯	⋯	⋯	⋯	⋯
5794951810577913216	263792500	235.07804	−71.56834	11.79	0.15	Gaia DR3	−1.0	9.95	HARPS	20.99	2.0
5772759096086560640	418807720	219.89375	−80.81085	11.75	4.94	Gaia DR3	⋯	⋯	⋯	0.66	0.0
6487693790194944128	234299628	358.67472	−61.587	40.4	0.31	Gaia DR3	⋯	⋯	⋯	6.24	1.0
5800510224109658240	260333394	225.01435	−67.55584	⋯	⋯	None	⋯	⋯	⋯	⋯	⋯
5269380721313848576	306931200	122.70793	−71.12608	11.74	5.48	Gaia DR3	⋯	⋯	⋯	0.64	0.0
6401084400282291200	372382536	317.05673	−66.38064	−7.61	0.32	Gaia DR3	⋯	⋯	⋯	21.09	2.0
5864837701762139776	449884234	201.30643	−64.48524	−4.8	0.13	Gaia DR3	0.0	10.0	Torres et al. (2006)	⋯	3.0
5864837697361427072	449884184	201.30292	−64.47922	⋯	⋯	None	⋯	⋯	⋯	⋯	⋯

8

Table 3
(Continued)

Gaia DR3	TIC	α J2016.0	δ J2016.0	RV (km s^{-1})	σ_{RV} (km s^{-1})	RV Source	EqW Li (mÅ)	σ_{EqWLi} (mÅ)	Li Source	P_{rot} (days)	Rotation Quality
6419363540577655552	268750176	280.07896	−71.75748	⋯	⋯	None	⋯	⋯	⋯	⋯	⋯
4798732668801919360	302964354	83.34074	−47.08869	−14.91	0.15	Gaia DR3	⋯	⋯	⋯	9.75	0.0
4703216410071320832	328011968	2.9732	−69.35424	⋯	⋯	None	⋯	⋯	⋯	⋯	⋯
5848941306174999424	293289676	222.03239	−65.90071	42.01	0.15	Gaia DR3	⋯	⋯	⋯	6.22	1.0
4810476659874420352	200363066	77.18555	−45.50202	17.54	0.28	Gaia DR3	⋯	⋯	⋯	6.97	1.0
4836664278068407680	101013663	55.79118	−43.53687	⋯	⋯	None	⋯	⋯	⋯	2.65	0.0
6427793736746396672	409887354	294.23901	−67.40906	8.07	0.5	Gaia DR3	⋯	⋯	⋯	12.1	2.0
4621748890580775040	391949832	79.17562	−80.81982	9.14	0.9	Gaia DR3	⋯	⋯	⋯	9.6	0.0
4814461079558759552	200460091	71.41374	−43.89702	25.32	0.14	Gaia DR3	120.0	22.0	Torres et al. (2006)	7.99	0.0
6638134365589225344	456618376	282.72856	−55.75472	⋯	⋯	None	⋯	⋯	⋯	1.66	0.0
6472232212871226240	1989423078	303.64768	−54.51718	⋯	⋯	None	⋯	⋯	⋯	0.57	0.0
5779453442570694656	407123648	234.58773	−78.05657	10.31	0.39	Gaia DR3	⋯	⋯	⋯	5.44	0.0
5849280505494491264	446339621	216.94617	−66.50214	7.35	2.68	Gaia DR3	⋯	⋯	⋯	0.56	0.0
4621599047761938688	260995123	78.98376	−81.07174	⋯	⋯	None	−4.0	9.8	HARPS	9.32	2.0
4957985696747200256	111267568	30.68873	−40.95115	3.23	0.13	Gaia DR3	1.0	10.05	HARPS	20.84	2.0
4957985696747200512	111267570	30.70091	−40.94715	2.57	18.86	Gaia DR3	⋯	⋯	⋯	⋯	⋯
4987736729049009024	183587880	16.89728	−41.7666	15.84	0.59	Gaia DR3	⋯	⋯	⋯	⋯	⋯
6428064697644127360	325070705	293.46493	−66.8089	−23.74	0.9	Gaia DR3	⋯	⋯	⋯	3.04	2.0
5778945223380267648	384150620	243.6151	−78.0851	9.34	0.24	Gaia DR3	⋯	⋯	⋯	6.53	0.0
4929504325499059840	158565951	20.72477	−49.8718	−22.66	2.94	Gaia DR3	⋯	⋯	⋯	6.76	2.0
6475208492064361216	100327960	307.33502	−51.49625	−9.92	4.45	Gaia DR3	⋯	⋯	⋯	0.28	0.0
5311011770618920832	385321596	137.79154	−55.03122	26.85	0.25	Gaia DR3	−1.0	9.95	HARPS	10.35	1.0
4931155036049677312	100100909	24.36671	−45.97411	⋯	⋯	None	⋯	⋯	⋯	0.18	1.0
5489939725890739072	294154590	107.74976	−56.54963	21.5	3.9	Malo et al. (2014)	⋯	⋯	⋯	0.19	0.0
6473160651658069120	201688405	300.55649	−54.43382	⋯	⋯	None	⋯	⋯	⋯	0.7	0.0
5347831082126227712	80677028	165.98173	−52.9771	21.72	0.22	Gaia DR3	⋯	⋯	⋯	10.35	1.0
5836174636208941184	424969508	240.61729	−56.855	−10.73	0.12	Gaia DR3	76.0	13.8	NRES	11.04	1.0
5489939730188462464	766616259	107.74932	−56.54943	23.2	2.7	Malo et al. (2014)	⋯	⋯	⋯	0.19	0.0
6568464361047484288	279314834	331.68828	−42.29003	⋯	⋯	None	⋯	⋯	⋯	⋯	⋯
5895473600324039680	412016542	214.60387	−55.47751	−17.75	0.38	Gaia DR3	⋯	⋯	⋯	3.26	0.0
4666870820559656320	31997119	55.57044	−70.48808	⋯	⋯	None	⋯	⋯	⋯	⋯	⋯
5924203182025615616	213471387	257.67238	−52.11216	−16.13	0.42	Gaia DR3	⋯	⋯	⋯	8.31	1.0
5485803711041321216	294272204	108.51836	−58.33321	22.54	5.21	Gaia DR3	⋯	⋯	⋯	0.36	0.0
6065158377962553344	241655722	207.77287	−53.73532	⋯	⋯	None	−3.0	9.85	HARPS	0.33	0.0
6382707266014366976	410150587	340.0304	−71.20608	8.12	7.64	Gaia DR3	⋯	⋯	⋯	1.52	0.0
5843122587538897920	329545966	192.05181	−70.64542	−2.55	0.39	Gaia DR3	⋯	⋯	⋯	8.11	0.0
5228172606059735936	295667714	171.55456	−71.657	4.9	2.15	Gaia DR3	⋯	⋯	⋯	0.15	1.0
5236626338671861760	280859868	173.26805	−66.93342	⋯	⋯	None	⋯	⋯	⋯	0.18	0.0
6471472278538182656	100662048	310.24591	−52.86164	1.09	0.41	Gaia DR3	⋯	⋯	⋯	8.66	1.0
5808631010846251264	1206158616	247.96385	−69.8877	6.8	0.6	Gaia DR3	⋯	⋯	⋯	⋯	⋯
6516607269516143488	121475280	343.01097	−45.92732	−20.2	1.5	Gaia DR3	⋯	⋯	⋯	⋯	3.0
6445000062927795456	411955564	290.6827	−61.73302	−8.03	1.61	Gaia DR3	⋯	⋯	⋯	3.67	2.0
6473378904715812608	101843377	304.09703	−53.81459	⋯	⋯	None	⋯	⋯	⋯	⋯	3.0
4807503271195302272	192790473	82.11748	−39.37089	27.62	0.18	Gaia DR3	90.0	14.5	NRES	8.51	0.0
4807503030677131392	192790476	82.14335	−39.37304	27.14	0.2	Gaia DR3	⋯	⋯	⋯	10.49	0.0
5784341905625638400	418250020	195.98006	−80.72364	⋯	⋯	None	⋯	⋯	⋯	2.32	0.0
5799237986096386176	261517097	227.10181	−69.9266	38.45	1.52	Gaia DR3	⋯	⋯	⋯	1.61	0.0

8

Table 3
(Continued)

Gaia DR3	TIC	α J2016.0	δ J2016.0	RV (km s^{-1})	σ_{RV} (km s^{-1})	RV Source	EqW Li (mÅ)	σ_{EqWLi} (mÅ)	Li Source	P_{rot} (days)	Rotation Quality
5212667151341318528	177255827	101.67769	−77.00024	18.84	2.27	Gaia DR3	⋯	⋯	⋯	6.16	0.0
5949144267577982720	30087015	264.89203	−45.98383	⋯	⋯	None	⋯	⋯	⋯	1.72	2.0
5830329666688142976	350798917	246.86026	−61.30937	−9.22	13.99	Gaia DR3	⋯	⋯	⋯	⋯	⋯
5808065209030685568	301096165	254.69636	−70.00533	⋯	⋯	None	⋯	⋯	⋯	0.12	2.0
5374565879145559424	162434199	169.61116	−47.36567	⋯	⋯	None	⋯	⋯	⋯	⋯	3.0
5844099503627340416	341055901	202.44755	−69.87024	1.72	2.13	Gaia DR3	⋯	⋯	⋯	10.02	2.0
6637448957528512128	1816965664	281.35069	−57.01822	−9.7	4.39	Gaia DR3	⋯	⋯	⋯	⋯	3.0
5808065209026675584	301096163	254.68868	−70.00536	⋯	⋯	None	⋯	⋯	⋯	⋯	⋯
4951967794731342464	91641297	40.1676	−39.8555	−8.13	0.12	Gaia DR3	0.0	10.0	HARPS	⋯	⋯
6638822694226428672	421985503	289.09009	−58.13617	⋯	⋯	None	⋯	⋯	⋯	0.82	2.0
5226155861208509440	454295341	166.98254	−74.3516	⋯	⋯	None	⋯	⋯	⋯	⋯	⋯
6361144915282549504	398383318	284.15387	−79.71561	−6.45	0.44	Gaia DR3	⋯	⋯	⋯	14.47	0.0
5544880780046222464	144355325	121.29768	−35.36725	27.98	2.24	Gaia DR3	⋯	⋯	⋯	0.59	0.0
6098895724014519936	129228711	220.85415	−44.4849	3.52	0.31	Gaia DR3	⋯	⋯	⋯	2.45	1.0
4812461514583738752	161637624	75.96187	−43.47932	25.74	0.55	Gaia DR3	⋯	⋯	⋯	0.19	0.0
6059555129283005824	271508756	186.82305	−57.96319	23.82	1.44	Gaia DR3	⋯	⋯	⋯	5.22	1.0
5307887302169199360	441850362	145.62191	−55.57533	−43.94	39.05	Gaia DR3	⋯	⋯	⋯	20.58	2.0
5499416283468435712	260131643	92.61806	−54.92268	73.45	0.53	Gaia DR3	⋯	⋯	⋯	2.99	2.0
5201153963224913152	454291823	166.88595	−77.47413	⋯	⋯	None	⋯	⋯	⋯	0.68	0.0
5212473847749416576	177352809	104.26012	−77.16416	⋯	⋯	None	⋯	⋯	⋯	⋯	⋯
5593952946066050304	151006728	118.33462	−33.4419	9.19	0.14	Gaia DR3	⋯	⋯	⋯	15.4	2.0
5440696864990921984	105882667	157.10331	−39.98972	25.42	2.16	Gaia DR3	⋯	⋯	⋯	0.64	0.0
5910453793394324096	306275682	264.70749	−62.8155	−0.81	12.06	Gaia DR3	⋯	⋯	⋯	0.32	1.0
5846665969920173440	449041310	215.56929	−69.08548	−5.3	0.17	Gaia DR3	⋯	⋯	⋯	6.53	1.0
5575275335880709760	393452839	94.60879	−36.9711	102.78	0.52	Gaia DR3	⋯	⋯	⋯	6.69	1.0
4663081800416386816	55559834	73.18483	−65.2817	68.23	4.84	Gaia DR3	⋯	⋯	⋯	1.09	0.0
5203361404618057984	453220734	146.30928	−77.88724	⋯	⋯	None	⋯	⋯	⋯	⋯	⋯
5816991972140661760	304074982	258.74004	−64.37733	−20.63	5.67	Gaia DR3	⋯	⋯	⋯	0.6	0.0
5549662762266400256	219164682	90.62517	−51.81968	19.3	6.65	Gaia DR3	⋯	⋯	⋯	0.57	0.0
4812970180447752832	200340962	76.89603	−42.0083	⋯	⋯	None	⋯	⋯	⋯	⋯	⋯
5793819146109422848	402682344	223.94074	−73.16681	10.5	0.13	Gaia DR3	31.0	11.55	NRES	1.84	0.0
4856812863008160256	165213021	56.50662	−36.96483	19.13	0.26	Gaia DR3	⋯	⋯	⋯	6.97	0.0
6810820947424835712	209375295	325.44577	−27.08304	−10.85	1.69	Gaia DR3	⋯	⋯	⋯	⋯	⋯
5609768282659317376	64540162	106.92959	−27.71274	−35.48	6.64	Gaia DR3	⋯	⋯	⋯	0.47	1.0
5814435195287770368	293075283	254.23528	−68.48423	⋯	⋯	None	⋯	⋯	⋯	0.44	0.0
5880617480245383168	416196764	223.40451	−58.28627	−3.73	3.19	Gaia DR3	⋯	⋯	⋯	⋯	3.0
5837977594661266688	360405963	188.37251	−75.38639	16.18	0.28	Gaia DR3	127.0	16.35	HARPS	5.44	0.0
4655505684288949888	30187438	73.81168	−68.64083	18.15	4.4	Gaia DR3	⋯	⋯	⋯	⋯	3.0
5348350154694000000	91474396	170.94489	−52.96087	4.13	0.41	Gaia DR3	⋯	⋯	⋯	5.67	0.0
2391670474561181440	9210746	352.55748	−20.39187	⋯	⋯	None	0.0	10.0	HARPS	7.63	2.0
5601615988055197952	127643940	117.24332	−27.08892	⋯	⋯	None	⋯	⋯	⋯	⋯	⋯
5795711199462066816	263191217	234.12269	−71.56552	3.63	7.83	Gaia DR3	⋯	⋯	⋯	0.71	2.0
5601266725623628416	776524223	119.80877	−26.62498	⋯	⋯	None	⋯	⋯	⋯	⋯	⋯
5974322293543549440	200105910	261.02843	−37.46552	−9.68	1.85	Gaia DR3	⋯	⋯	⋯	8.01	2.0
6474015178351213824	100273626	307.12998	−53.61092	−4.68	1.51	Gaia DR3	⋯	⋯	⋯	9.02	0.0
6443749334090478976	1988709541	300.27412	−60.37428	−4.17	3.11	Gaia DR3	⋯	⋯	⋯	0.82	0.0
6035956895316486656	1255391268	240.48347	−33.95344	−27.31	1.19	Gaia DR3	⋯	⋯	⋯	2.96	2.0

Table 3
(Continued)

Gaia DR3	TIC	α J2016.0	δ J2016.0	RV (km s^{-1})	$\sigma_{\rm RV}$ (km s^{-1})	RV Source	EqW Li (mÅ)	$\sigma_{\rm EqWLi}$ (mÅ)	Li Source	$P_{\rm rot}$ (days)	Rotation Quality
6035956925371144832	1255391255	240.4837	−33.95334	−27.25	0.59	Gaia DR3	⋯	⋯	⋯	2.96	2.0
5601950690575573120	776770284	118.47594	−26.86299	⋯	⋯	None	⋯	⋯	⋯	⋯	⋯
5920596066603197056	76392634	269.69148	−55.02187	⋯	⋯	None	⋯	⋯	⋯	⋯	⋯
5782666490422418816	357665438	188.51063	−83.53518	⋯	⋯	None	⋯	⋯	⋯	⋯	⋯
5614014978832904832	779943454	115.97402	−25.43424	⋯	⋯	None	⋯	⋯	⋯	⋯	⋯
4988735051246293504	183596242	18.36797	−38.35104	14.3	0.5	Malo et al. (2014)	⋯	⋯	⋯	⋯	⋯
2395031273585836288	434103018	353.20741	−16.84662	−1.14	0.13	Gaia DR3	0.0	10.0	HARPS	10.09	0.0
6635630910753507968	119337122	276.29233	−59.01216	⋯	⋯	None	⋯	⋯	⋯	⋯	⋯
4762827532481570432	382066186	79.61502	−58.47309	6.98	0.57	Gaia DR3	⋯	⋯	⋯	2.38	2.0
5811333301184104320	293802706	263.43478	−69.31955	44.38	0.59	Gaia DR3	⋯	⋯	⋯	13.11	2.0
2966316109264052096	160301040	88.62609	−19.70445	42.46	0.12	Gaia DR3	8.0	10.4	HARPS	5.54	0.0
5204815332648173440	453595277	155.58719	−75.16585	19.48	0.47	Gaia DR3	⋯	⋯	⋯	7.9	0.0
6566592270703002496	88273820	333.23474	−46.46388	24.1	3.85	Gaia DR3	⋯	⋯	⋯	⋯	3.0
5455707157211784832	188043641	160.8667	−29.06451	22.57	0.13	Gaia DR3	156.0	17.8	HARPS	6.9	0.0
5825336750035914624	455606289	229.65218	−64.46337	6.75	0.23	Gaia DR3	⋯	⋯	⋯	8.91	0.0
6788656957673130112	289934729	318.16972	−29.37232	⋯	⋯	None	⋯	⋯	⋯	⋯	⋯
5217796343023874432	452475180	139.65738	−73.8369	⋯	⋯	None	⋯	⋯	⋯	0.67	0.0
5494935911023714944	260267208	93.91221	−57.70134	27.35	0.23	Gaia DR3	140.0	17.0	HARPS	3.68	0.0

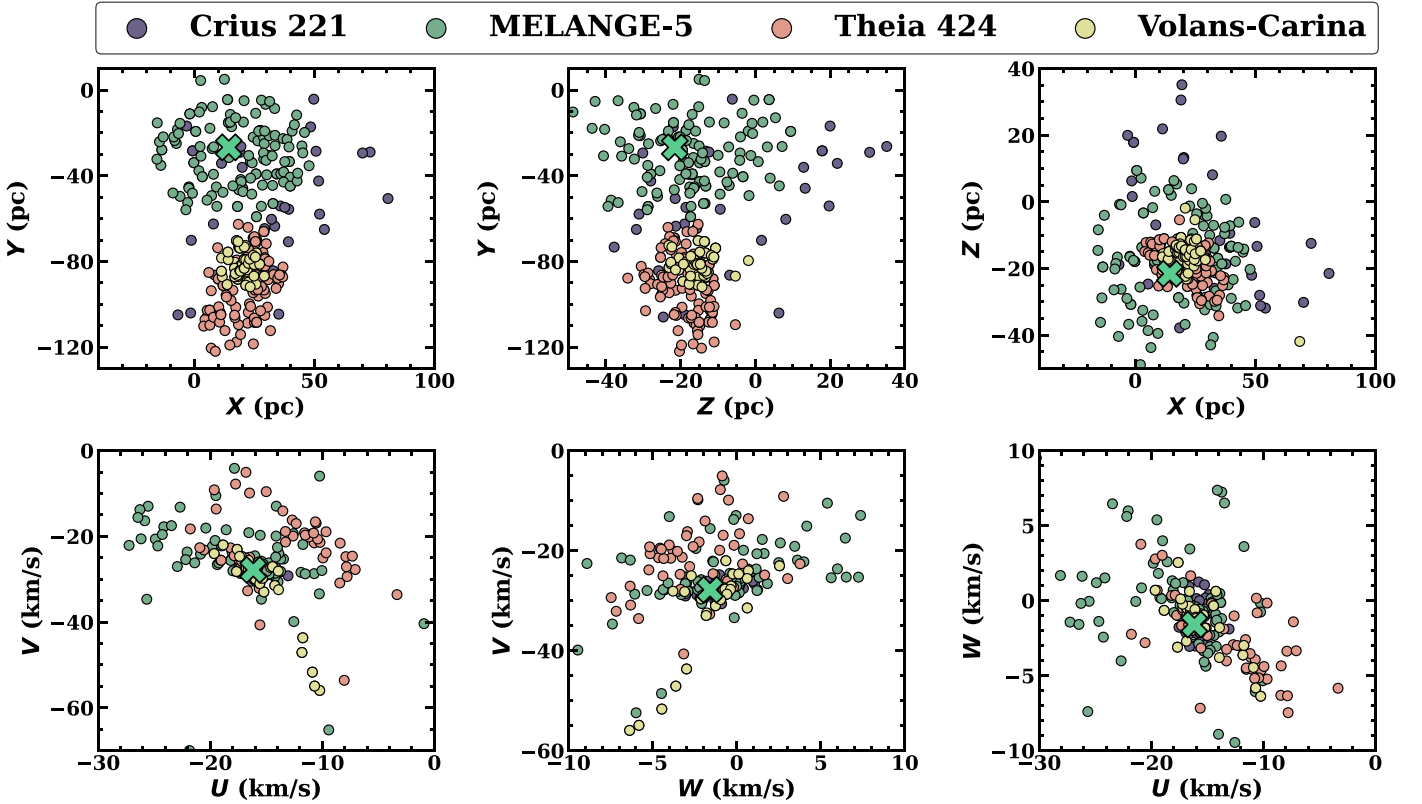(This table is available in machine-readable form.)

Figure 6. The spatial spread and velocity spread of MELANGE-5 (green) compared to the nearby associations, Crius 221 (purple), Theia 424 (pink), and Volans-Carina (yellow). The top row shows the galactic position (*X*, *Y*, and *Z*), and the bottom row shows the velocities (*U*, *V*, and *W*) for each population. MELANGE-5 (∼200 Myr) overlaps with Crius 221 (∼100 Myr) but does not intersect with Theia 424 or Volans-Carina. The position of TOI-1224 is marked with a green cross.

used the effective temperature scale from Curtis et al. (2020), the same extinction corrections and intrinsic age scale for these clusters as listed in Table 1 of Bouma et al. (2023), and the data behind the relevant figure from Bouma et al. (2023). The most relevant assumed ages are those for the Pleiades (Galindo-Guil et al. 2022) and NGC 3532 (Fritzewski et al. 2019). We assumed negligible reddening for MELANGE-5 due to its proximity and only plot the stars in the association with $3800 < T_{eff}/K < 6200$, which are most diagnostic for the rotation-based age.

Visually, Figure 4 shows that, on average, the association of MELANGE-5 falls above the 120 Myr clusters and slightly below the 300 Myr clusters. For any individual star, this measurement would not be particularly significant. However, the ensemble of stars falling above the 120 Myr sequence is highly significant because almost every ≈G2–K4 star falls above it, and this is the regime with the most diagnostic power. To leverage the ensemble information, we use the hierarchical Bayesian framework implemented in gyro − interp and discussed by Bouma et al. (2023). This model assumes that the intrinsic age of any star in the association is drawn from a Gaussian with an unknown mean and intrinsic scatter. We considered two subsets of the rotation data when performing the inference: (i) all stars with $3800 < T_{eff}/K < 6200$ and (ii) only the "good" rotation periods. These assumptions yielded a mean cluster age and associated $1 - \sigma$ uncertainties of $t = 283^{+92}_{-59}$ Myr when considering all rotation periods and 234^{+77}_{-56} Myr when only considering the "good" periods. Both estimates agree with the visual impression from Figure 4 that MELANGE-5 is between the 120 and 300 Myr calibration sequences. The statistical uncertainty on this statement is
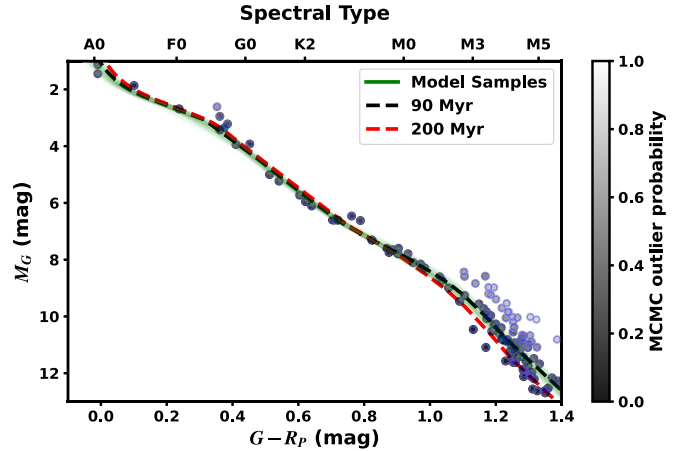

Figure 7. CMD of members of Theia 424 from Kounkel et al. (2020) compared to PARSECv1.2 solar metallicity models using a mixture model (Section 4.1.3). The green lines are 100 random draws from the fit posterior, and individual points are shaded by the probability that they are part of the main (single-star single-aged) population. The group is well described by a ≃90 Myr isochrone (black dashed line) with a visible binary sequence above and a small number of field interlopers below.

limited by the intrinsic astrophysical scatter in the cluster rotation sequences at these ages.

4.1.3. Isochronal Age

We compared Gaia photometry of candidate MELANGE-5 members to predictions from the PARSECv1.2 isochrones (Bressan et al. 2012). We used the mixture model described in the Appendix of Mann et al. (2022), which follows the statistical
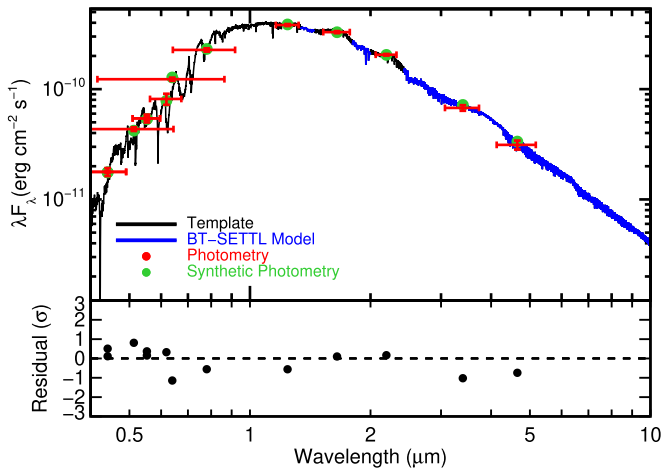
Figure 8. SED of TOI-1224 (red points) compared to the best-fit template spectra (black) and BT–SETTL model (blue). Horizontal errors on the observed photometry approximate the filter width. The synthetic photometry used to compare to the observed photometry is shown as green points. The bottom panel shows the residual in units of standard deviations.

Table 4
Age Determinations

Method	Age (Myr)
Lithium (Eagles)	185 ± 35
Isochrone (PARSEC)	$150-800$
Gyrochronology	283^{+92}_{-59}
Variability	176^{+98}_{-51}
Adopted	210 ± 27

age of 176^{+98}_{-51} Myr, which is consistent with our other age determination methods.

4.1.5. Combined Age

Our four methods for estimating the age of MELANGE-5 are mostly independent of each other in that they rely on different data sets and approaches. They do rely on a common set of members, but each method is relatively robust to the exact membership list. Gyrochronology, lithium, and Gaia excess variability are also calibrated on a similar set of clusters, although the underlying cluster population ages are known more precisely than the determinations here. Hence, we can combine these ages into one more precise age.

We find an adopted age by maximum likelihood, assuming (asymmetric when required) Gaussians except for the isochrone age, for which we assume a uniform distribution from 150 to 800 Myr. We estimate the age for MELANGE-5 to be 210 ± 27 Myr. We adopt this value for the age of the group. A summary of each age determination can be found in Table 4.

4.2. Membership List Contamination Rate

Following Barber et al. (2022), we can estimate the fraction of interlopers using the Gaia RVs. As explained in Section 3.1, the target list was selected based on position and tangential velocity. Since the probability of RV alignment is small, the fraction of stars with inconsistent velocities is a rough estimate of the fraction of stars that are field contaminants. However, tight binaries (which may have discrepant velocities) could be falsely assigned as nonmembers, increasing the contamination rate, and field stars that align with the group by chance could be falsely flagged as members, decreasing the contamination rate.

We assumed all stars with 3σ consistent RVs are members and adopt an internal velocity dispersion of $0-3$ km s^{-1} along the line of sight. This yielded a contamination fraction of 38%–55% (the high value corresponding to the lowest assumed velocity dispersion). Assuming that TOI-1224 is 2 km s^{-1} off from the true group center (as suggested by Figure 2) decreases the contamination to 28%–40%.

The lithium suggests a similar contamination fraction. Focusing on those stars where we expect a lithium detection (i.e., $0.6 < B_P - R_P < 1.3$), there were 18 stars with data, and 12 of them (67%) showed elevated lithium levels consistent with the age of the group (see Figure 3), for a contamination rate of 33%. As with RVs, this may include nonmembers with elevated lithium by chance and exclude some members that are depleted due to astrophysical variation (Somers & Stassun 2017).

The rotation periods yield a similar estimate. Of the 159 candidate members, 34 of them were too faint or had contamination too high for a useful TESS light curve. Of the remaining, 81 stars had rotation periods consistent with membership. Most of the rest had no clear rotation (Q3 or
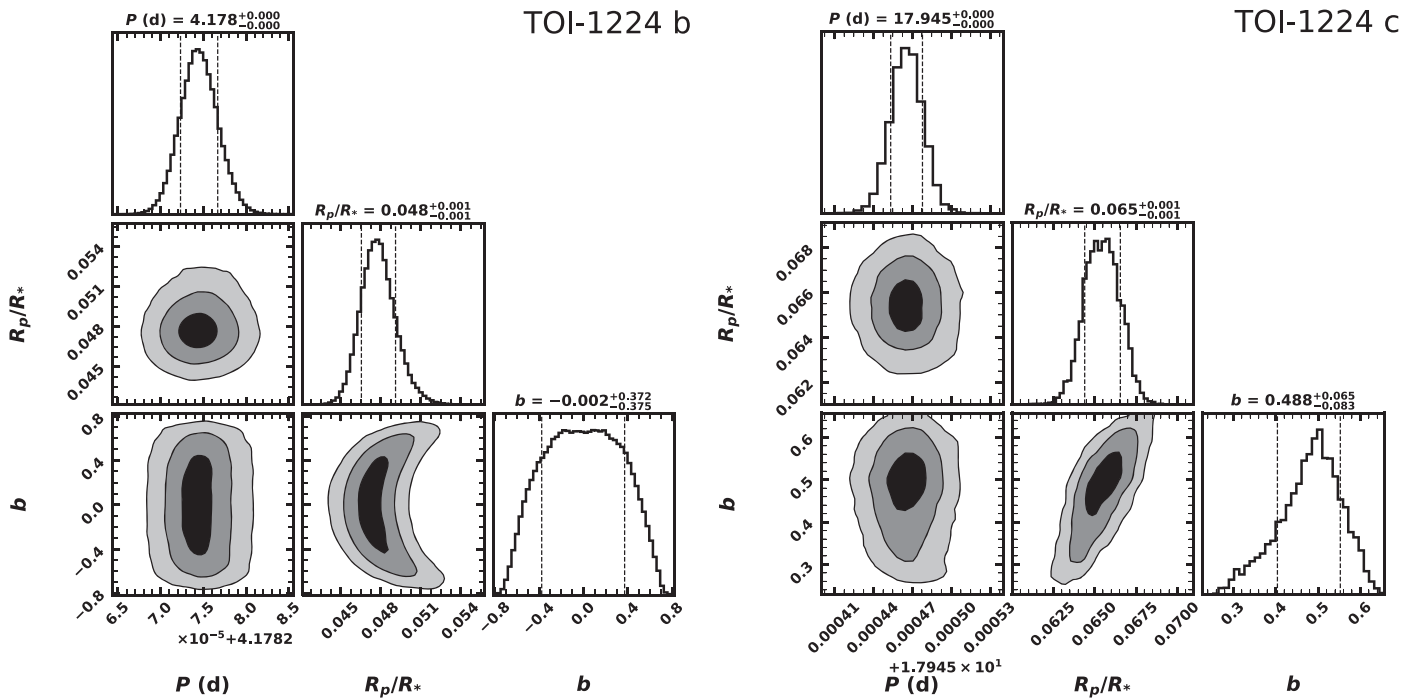
methods from Hogg et al. (2010). To summarize, the model is a mixture of two models. The first represents a single-aged single-star population and is drawn from the isochrones as a function of age (τ) and reddening ($E(B - V)$). The second is meant to capture outliers (mostly nonmembers) and is described by an offset from the isochrone model (Y_B) and a Gaussian variance around that offset (V_B). The final parameter (f) captured missing uncertainties such as variation in reddening between members, model systematics, and underestimated uncertainties in the Gaia data.

For our comparison, we excluded stars with a renormalized unit weight error (RUWE) >1.5 (Ziegler et al. 2020; Wood et al. 2021), those with Gaia photometry or parallax SNR < 20, and those outside the model grid photometry (including white dwarf candidates). The mixture model can handle some of the stars eliminated by these cuts by calling them outliers, but a less complex outlier population tends to provide better fits (e.g., including white dwarfs biases the outlier distribution). The fit was run using emcee (Foreman-Mackey et al. 2013) with 30 walkers for 20,000 steps, which was more than sufficient for convergence.

As shown in Figure 5, the CMD fit provides only large bounds on the age of MELANGE-5. The minimum age is set by the lack of pre-main-sequence M dwarfs ($\simeq 150$ Myr for cooler than M5) and the maximum age by the lack of post-main-sequence evolution in the F stars (approximately 800 Myr). The younger limit is set primarily by just four stars that sit below the 150 Myr sequence.

4.1.4. Age from Gaia Excess variability

Barber & Mann (2023) presented a method to estimate the age of an association from the excess variance in Gaia photometry (Riello et al. 2021). The method uses a Skumanich-like relation between stellar activity and age and takes advantage of the fact that more variable sources will have higher photometric uncertainties than their quiet counterparts. The method considers the distribution of variability over a population of coeval stars, thereby averaging over stellar inclinations and star-to-star variability. Using the open-source code Excess Variability-based Age,[36] this technique yielded an

---

[36] ○ https://github.com/madysonb/EVA

Figure 9. Posteriors from the MCMC fit for the parameters, period (P), planet-to-star radius ratio (R_P/R_*), and impact parameter (b) for planet b (left) and planet c (right). Planet b was fit using `MISTTBORN`, and planet c was fit using `juliet` to account for the TTVs. In the histogram, the dashed lines indicate the 16th and 84th percentiles. Figure made with `corner.py` (Foreman-Mackey 2016).

Q4; 38), with six Q0 or Q1 rotators landing clearly above the color–period sequence (Figure 4). This gives a contamination fraction of 35%. Using rotation periods in this way has similar issues to lithium and velocities; some nonmembers will match by chance, some members will have no apparent rotation because they are pole-on, and some rotation periods may appear discrepant or match because we actually measured an alias of the true period.

Overall, these three methods yield a similar result, suggesting that about 35% of the stars in our target list are field stars. All three calculations may be underestimates due to contamination from the nearby 90 Myr population(s) (Section 4.3). These stars will be closer in RV than random field stars, rotate faster, and have elevated lithium levels. However, the lack of pre-main-sequence M dwarfs in the MELANGE-5 CMD suggests that contamination from these younger groups is relatively low.

4.3. Relation to Crius 221, Volans-Carina, and Theia 424

Moranta et al. (2022) include TOI-1224 in the list of Crius 221 members[37] and also suggest that Crius 221 is part of Volans-Carina (Gagné & Faherty 2018), Theia 424 (Kounkel et al. 2020), and Oh 30 (Oh et al. 2017). Indeed, all of these groups (and MELANGE-5) show significant spatial and kinematic overlap (Figure 6). This raises the question of if MELANGE-5 is a unique group or an extension of these known populations.

If all groups are part of a common parent population, they should have the same age. However, Gagné & Faherty (2018) found that Volans-Carina is only 89^{+5}_{-7} Myr, which is inconsistent with our age estimate for MELANGE-5. As an additional check, we reran our isochronal fit described in

Section 4.1.3 on Crius 221, Volans-Carina, and Theia 424 (Oh 30 had too few members to test). For consistency, the method was unchanged from our analysis of MELANGE-5. Using the PARSEC models, we measured ages of 98^{+23}_{-9} Myr, 93 ± 10 Myr, and 99^{+7}_{-12} Myr for Crius 221, Volans-Carina, and Theia 424, respectively. Crius 221 only has two stars passing our selection criteria later than M3 (where we expect pre-main-sequence stars at this age); if both are binaries, the age could be significantly older. However, the assigned ages of the other two are more robust to the target list. Theia 424 in particular matches the 90–100 Myr isochrone, has a clearly separated binary sequence (Figure 7), and includes a smaller population of likely main-sequence mid-M interlopers.

We conclude that although these groups overlap with MELANGE-5, they are likely distinct populations.

4.4. Membership of TOI-1224

A separate question is the membership of TOI-1224. The target is unambiguously young, but there is some ambiguity about which group it resides within. TOI-1224 is spatially separate from Theia 424/Volans-Carina (Figure 1) and is not listed as a member of either. It is, however, listed as a member of Crius 221. By design, TOI-1224 is at the center of MELANGE-5. Selecting any of the other high-probability members (stars showing high lithium and rotation) and rerunning `Comove` includes TOI-1224 as a nearby member.

Most likely, TOI-1224 is part of either Crius 221 or MELANGE-5. Moranta et al. (2022) refer to Crius 221 as a corona of Volans-Carina; however, it is quite diffuse compared to the other groups considered here. It may be some mix of Volans-Carina and MELANGE-5. Assuming Crius 221 is a distinct association, the strongest piece of evidence that TOI-1224 is a member is the target's CMD position, which is a marginally better match to a 90 Myr isochrone than 200 Myr. The difference is

---

[37] They specifically noted the planet host (TOI) as a planet in their newly identified group.

Table 5
Properties of the Host Star TOI-1224

Parameter	Value	Source
	Identifiers	
Gaia	4620009665047355520	Gaia DR3
TIC	299798795	Stassun et al. (2018)
2MASS	J02284641−8053571	Cutri et al. (2003)
ALLWISE	J022847.15−805356.9	ALLWISE
	Astrometry	
α	37.19797662402810	Gaia DR3
δ	−80.89910153220920	Gaia DR3
μ_α (mas yr^{-1})	159.965 ± 0.022	Gaia DR3
μ_δ (mas yr^{-1})	27.171 ± 0.022	Gaia DR3
π (mas)	26.827 ± 0.018	Gaia DR3
	Photometry	
G_{Gaia} (mag)	12.768 ± 0.0029	Gaia DR3
BP_{Gaia} (mag)	14.176 ± 0.006	Gaia DR3
RP_{Gaia} (mag)	11.601 ± 0.005	Gaia DR3
B (mag)	15.513 ± 0.09	UCAC4
V (mag)	13.950 ± 0.02	UCAC4
R (mag)	13.604 ± 0.05	UCAC4
g' (mag)	14.697 ± 0.04	UCAC4
r' (mag)	13.336 ± 0.03	UCAC4
i' (mag)	12.014 ± 0.07	UCAC4
J (mag)	10.018 ± 0.023	2MASS
H (mag)	9.405 ± 0.024	2MASS
K_S (mag)	9.134 ± 0.019	2MASS
W1 (mag)	9.036 ± 0.022	ALLWISE
W2 (mag)	8.890 ± 0.019	ALLWISE
W3 (mag)	8.758 ± 0.023	ALLWISE
	Kinematics and Position	
RV_{Bary} (km s^{-1})	14.63 ± 1.92	Gaia DR3
U (km s^{-1})	−16.16 ± 0.74	This work
V (km s^{-1})	−27.81 ± 1.38	This work
W (km s^{-1})	−1.59 ± 1.11	This work
X (pc)	14.437 ± 0.010	This work
Y (pc)	−26.759 ± 0.018	This work
Z (pc)	−21.565 ± 0.015	This work
	Physical Properties	
P_{rot} (days)	1.230	This work
$v \sin i_*$ (km s^{-1})	22.1 ± 1.2	This work
i_* (deg)	>82	This work
F_{bol} (×10^{-8} erg cm^{-2} s^{-1})	0.046 ± 0.001	This work
T_{eff} (K)	3326 ± 66	This work
M_* ($M_\odot$)	0.400 ± 0.010	This work
R_* ($R_\odot$)	0.404 ± 0.012	This work
L_* ($L_\odot$)	(2.01 ± 0.04) × 10^{-2}	This work
ρ_* ($\rho_\odot$)	4.86 ± 0.66	This work
Age (Myr)	210 ± 27	This work

Table 6
Priors on Limb-darkening Coefficients

Filter	g_1	g_2
TESS	0.272 ± 0.08	0.317 ± 0.04
z_s	0.232 ± 0.08	0.330 ± 0.04
g_P	0.533 ± 0.08	0.299 ± 0.04

Note.
Limb-darkening priors are provided as the traditional linear and quadratic terms but were fit using triangular sampling terms.

Table 7
Parameters of TOI-1224 b

Description	Parameter	b
	Fit Parameters	
First mid-transit midpoint	T_0 (BJD)	$2458327.70236^{+0.00055}_{-0.00054}$
Orbital period	P (days)	$4.1782745^{+2.2\times10^{-6}}_{-2.1\times10^{-6}}$
Planet-to-star radius ratio	$R_P/R_\star$	$0.0478^{+0.0013}_{-0.0012}$
Impact parameter	b	$0.27^{+0.22}_{-0.18}$
Stellar density	$\rho_\star$ ($\rho_\odot$)	$5.19^{+0.55}_{-1.0}$
TESS limb-darkening coefficient	q_1	$0.416^{+0.094}_{-0.089}$
TESS limb-darkening coefficient	q_2	$0.276^{+0.071}_{-0.072}$
LCO z_s limb-darkening coefficient	q_1	0.320 ± 0.110
LCO z_s limb-darkening coefficient	q_2	$0.202^{+0.077}_{-0.076}$
LCO g_p limb-darkening coefficient	q_1	0.750 ± 0.120
LCO g_p limb-darkening coefficient	q_2	0.297 ± 0.054
	GP Parameters	
Log period	$\log(P_{GP})$	$1.9^{+0.54}_{-0.45}$
Log variability amplitude	$\log(Amp)$	$-9.841^{+0.053}_{-0.052}$
Quality factor of main period oscillator	$\log(Q_1)$	$0.5022^{+0.0033}_{-0.0015}$
	Derived Parameters	
Ratio of semimajor axis to stellar radius	$a/R_\star$	$18.9^{+0.64}_{-2.0}$
Inclination	i (deg)	$89.19^{+0.56}_{-0.8}$
Transit depth	δ (%)	$0.228^{+0.013}_{-0.011}$
Planet radius	R_P ($R_\oplus$)	$2.104^{+0.094}_{-0.091}$
Semimajor axis	a (au)	$0.0355^{+0.0017}_{-0.0034}$
Equilibrium temperature[a]	T_{eq} (K)	$541.0^{+26.0}_{-14.0}$

Note.
[a] Assumes an albedo of 0.

membership with MELANGE-5. We briefly discuss in Section 7 what impact this has on the system parameters.

5. Properties of TOI-1224

5.1. M_* and R_* from Empirical Relations

We estimated stellar mass and radius using the empirical M_K–R_* and M_K–M_* relations from Mann et al. (2015) and Mann et al. (2019),[38] respectively. We used the relations without metallicity as a parameter, although using [Fe/H] = 0 yielded consistent results. For M_{K_S}, we used the parallax from Gaia DR3 and K_S photometry from the Two Micron All Sky Survey (2MASS; Skrutskie et al. 2006). We ignored the effects

small and is consistent with intrinsic scatter in the CMD (Section 4.1.3). The mixture model finds a 99.4% chance that TOI-1224 is part of the main population, although this is misleading because it only compares the probability that the star is part of MELANGE-5 to that of nonmembers (mostly the field). Indeed, a fit to the Crius 221 group using the same code finds a similar (99.1%) probability. As an M dwarf, the lack of lithium and fast rotation period for TOI-1224 are consistent with both 90 Myr and 200 Myr. Thus, we cannot rule out that TOI-1224 is part of Crius 221, but the kinematics and position favor

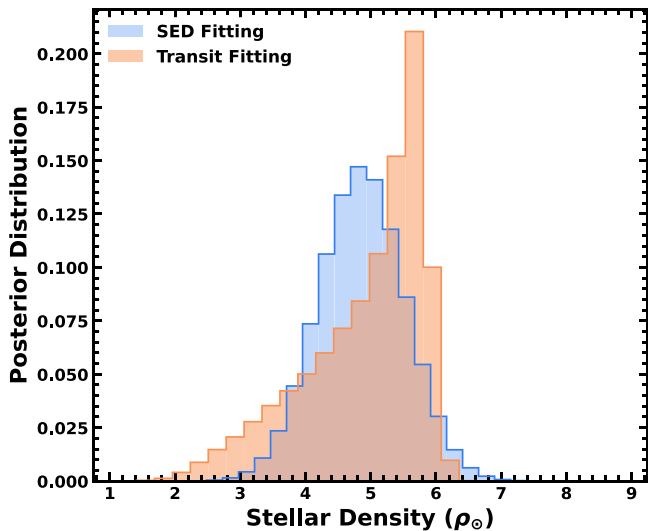---

[38] ⌂ https://github.com/awmann/M_-M_K-

Figure 10. Stellar density from SED fitting (blue) compared to the stellar density from the transit fit (orange) assuming the eccentricity is 0. This is consistent with a low or zero eccentricity for TOI-1224 b, which is common for (older) multiplanet systems (Van Eylen et al. 2019).

of extinction, as the star is within the Local Bubble. This yielded a radius of 0.404 ± 0.012 $R_{\oplus}$ and a mass of 0.400 ± 0.010 $M_{\oplus}$.

Uncertainties in M_* and R_* account for both measurement errors (in K_S and parallax) and uncertainties in the calibrations. While high activity may change the inferred or true parameters of stars (e.g., Feiden & Chaboyer 2012), there is no evidence that the M_K–R_* and M_K–M_* relations used here are inaccurate for active main-sequence stars (Mann et al. 2015, 2019). However, the age of TOI-1224 puts it near the zero-age main sequence, suggesting it could be pre-main-sequence depending on the model grid and assumed age. Correcting for this would yield a lower mass and larger radii, but the change is expected to be comparable to the measurement uncertainties in both cases. As an additional check, we estimated R_* from the spectral energy distribution (SED) below.

5.2. T_{eff}, L_*, and R_* from the SED

We fit the SED of TOI-1224 following the method in Mann et al. (2016b) but (as above) ignoring the effects of extinction and using templates instead of a flux-calibrated spectrum. To summarize, we compared photometry summarized in Table 5 to a grid of flux-calibrated templates from Mann et al. (2013) and Gaidos et al. (2014). The templates spanned 0.4–2.4 μm, and we used PHOENIX BT-SETTL atmosphere models (Allard et al. 2013) beyond these limits or in regions of high telluric contamination (see Figure 8). We also tested SPHINX model spectra (Iyer et al. 2023), which did a better job reproducing the template spectra but resulted in a negligible change to the final F_{bol} and T_{eff}. The result was an absolutely calibrated spectrum, which we used to compute F_{bol} by integrating the spectrum with wavelength. We turned this into L_* using the Gaia DR3 parallax. We estimated T_{eff} from the BT-SETTL model fit against the template and photometry as part of the comparison (the model selection is a free parameter). Finally, we estimated R_* from these parameters using the Stefan–Boltzmann relation.

The final error analysis accounted for errors in template choice, systematics in estimating the T_{eff} of M dwarf models (Mann et al. 2013), shape errors in the templates, and errors in the parallax and observed photometry. The final fit yielded

$T_{eff} = 3326 \pm 66$ K, $F_{bol} = (4.6 \pm 0.1) \times 10^{-10}$ erg cm^{-2} s^{-1}, $L_* = 0.0201 \pm 0.0004$ $L_{\odot}$, and $R_* = 0.435 \pm 0.019$ $R_{\odot}$. The final radius is consistent with the value estimated from the M_K–R_* relation in Section 5.1. These parameters are also consistent with those in the TESS Input Catalog (TIC; Stassun et al. 2019). This is expected, as the methods used for the TIC M dwarfs are similar to those employed here (Muirhead et al. 2018). Our adopted parameters are listed in Table 5.

5.3. Stellar Inclination

It is possible to test whether the stellar spin and planetary orbit are in alignment by converting estimates of $v \sin i_*$, P_{rot}, and R_* into an estimate of the stellar inclination (i_*). A simplified version of this conversion can be done by estimating the equatorial velocity (V) in $v \sin i_*$ using $V = 2\pi R_*/P_{rot}$. In practice, this requires additional statistical corrections, including the fact that we can only measure alignment projected onto the sky. To this end, we followed the formalism from Masuda & Winn (2020). The resulting stellar inclination was consistent with alignment with the planet, yielding a limit of $>75°$ at 95% and $>82°$ at 68%.

6. Transit Analysis

6.1. Identification of the Transit Signals

The inner planet, TOI-1224.01, was first detected in a joint transit search of TESS Sectors 1 and 13 as part of the SPOC search using an adaptive, wavelet-based matched filter (Jenkins 2002; Jenkins et al. 2010, 2020). The candidate passed all performed diagnostic tests (Twicken et al. 2018) and was fitted with an initial limb-darkened transit model (Li et al. 2019). The difference image centroid test located the host star within $3.''0 \pm 2.''9$ of the transit source, which was further constrained to $1.''3 \pm 2.''6$ in a search of Sectors 1–39. The TESS Science Office reviewed the diagnostic test results and issued an alert for this planet candidate as a TESS object of interest (TOI) on 2019 August 26 (Guerrero et al. 2021).

This particular case posed challenges for the SPOC due to stellar oscillations, as the pipeline is specifically designed to handle colored broadband noise. To address this, we refrained from identifying and removing sinusoidal harmonics, a technique applied in Kepler missions, as it tended to inadvertently eliminate energy from transit signatures, particularly those with shorter periods. Notably, the first transit of TOI-1224 c identified by the SPOC in Sector 68 is 102 orbital periods after the epoch for this planet in the manuscript. However, this discovery was after the identification of planet c through a custom search, as elaborated below.

We searched for additional planets using the Notch and LoCoR pipelines (N&L). N&L is described in further detail in Rizzuto et al. (2017)[39] and has been used widely to search for young planets in light curves from Kepler (e.g., Barber et al. 2022), K2 (e.g., Mann et al. 2017), and TESS (e.g., Rizzuto et al. 2020).

In addition to the original planet at 4.178 days, we identified an additional transit-like signal at 17.945 days with high SNR (72) when including all TESS data. The only other signals that passed our SNR threshold (>13) were rejected as clear aliases of the other two planets.

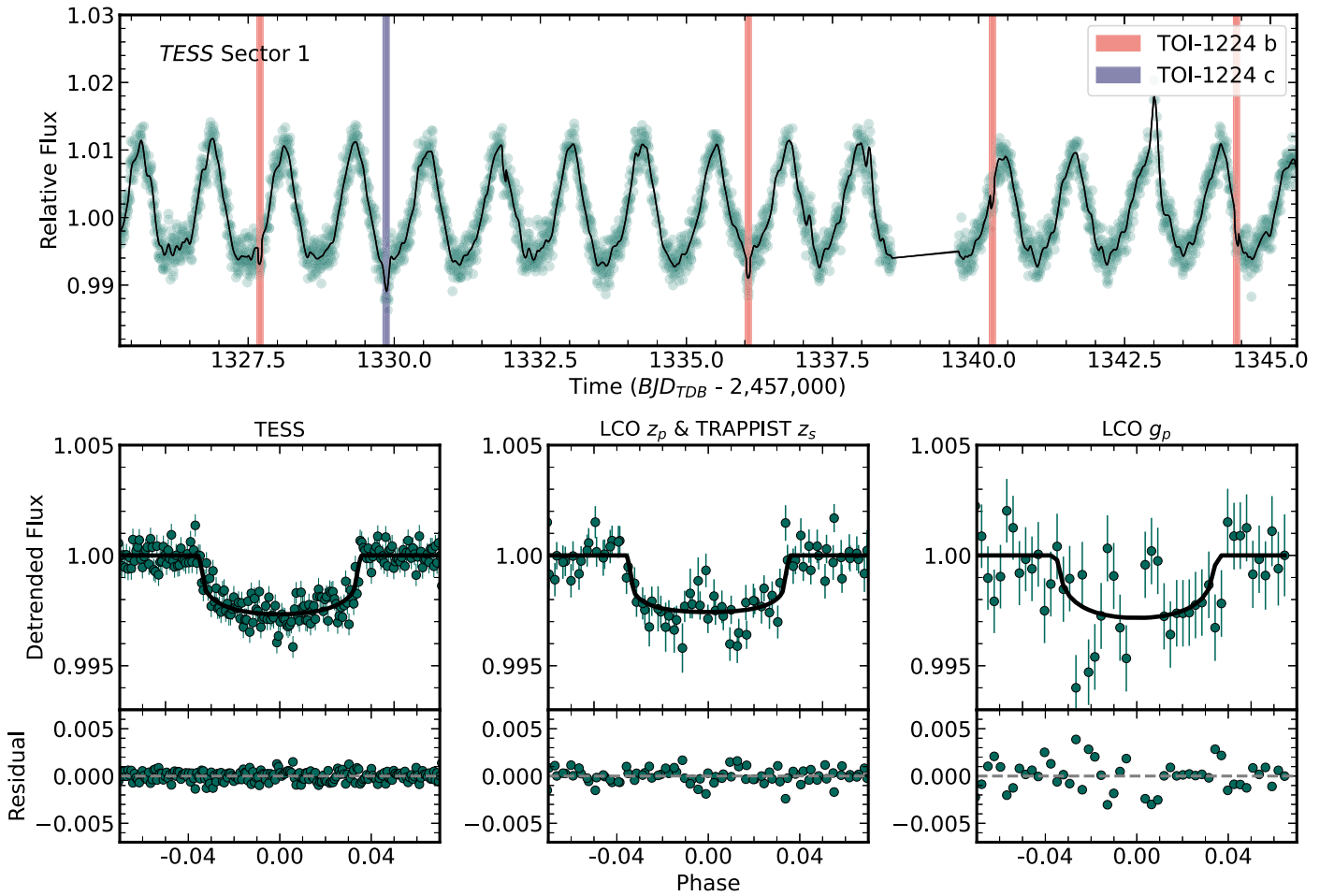[39] ⊙ https://github.com/arizzuto/Notch_and_LOCoR

Figure 11. The TESS Sector 1 light curve (green points) is binned to 5 minute intervals and is overplotted with a GP for the stellar variability (black line). Only ttransit of planet b is modeled here. The transit times of the two planets are marked in pink for TOI-1224 b and purple for TOI-1224 c. Bottom: phase-folded light curve of planet b after the best-fit stellar variability model has been removed taken in filters TESS, z, and g_p. Data for TESS and z are binned into 10 and 5 minute bins, with the best-fit transit model illustrated by a black line.
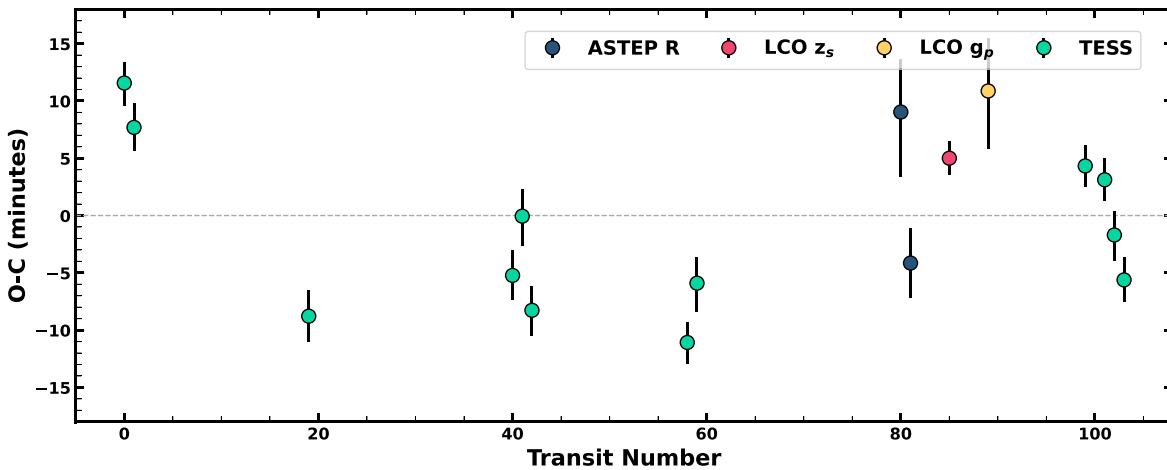
Figure 12. Observed minus calculated ($O - C$) mid-transit times as a function of time for TOI-1224 c in minutes taken with TESS (green), ASTEP R (purple), LCO z_s (red), and LCO g_p (yellow). The gray dashed horizontal line represents a linear ephemeris.

6.2. TOI-1224 b Planet Parameters

We used MCMC Interface for Synthesis of Transits, Tomography, Binaries, and Others of a Relevant Nature (MISTTBORN)[40] to fit the transit photometry for planet b.

---

[40] ⬡ https://github.com/captain-exoplanet/misttborn

MISTTBORN was first detailed in Mann et al. (2016a), with significant expansion detailed in Johnson et al. (2018). It uses BATMAN (Kreidberg 2015) for generating the model light curves, emcee (Foreman-Mackey et al. 2013) to explore the transit parameter space using an affine-invariant MCMC algorithm, and celerite (Foreman-Mackey et al. 2017a) to model the stellar variability with a Gaussian process (GP).
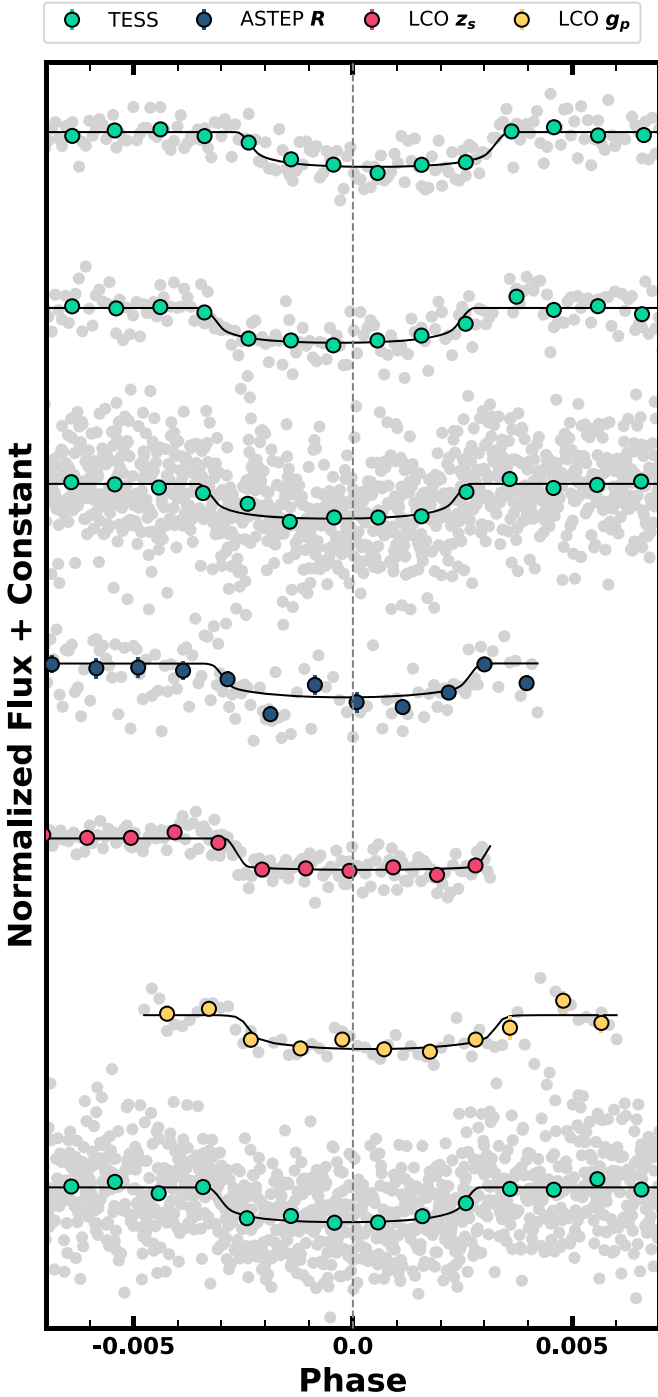
Figure 13. Phase-folded light curve of TOI-1224 c taken with TESS (green), ASTEP R (blue), LCO z_s (red), and LCO g_p (yellow). Transit numbers 0, 19, 58, 81, 85, 89, and 103 are arranged from top to bottom and offset for clarity. The best-fit transit model is overlaid as a black line. Circular points are data binned into 1.5 minute intervals.
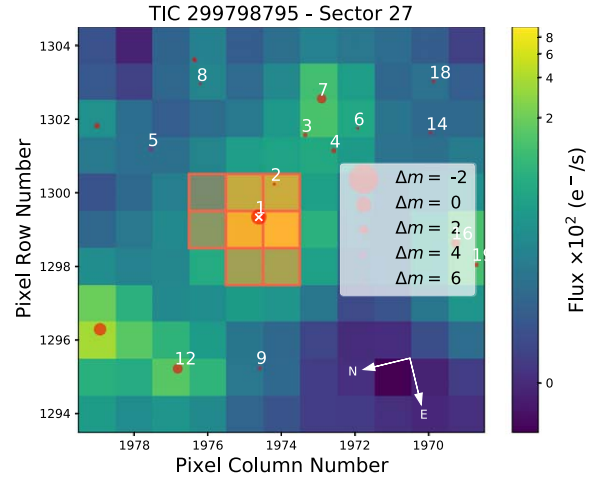

Figure 14. TESS image around TOI-1224 from Sector 13. The red region shows the aperture used for extracting the light curve. Points indicate other sources detected from Gaia scaled in size by their contrast. Other than TOI-1224, only a single Gaia source is within the aperture, and it is too faint to reproduce the transits. Figure made with `tpfplotter` (Aller et al. 2020).
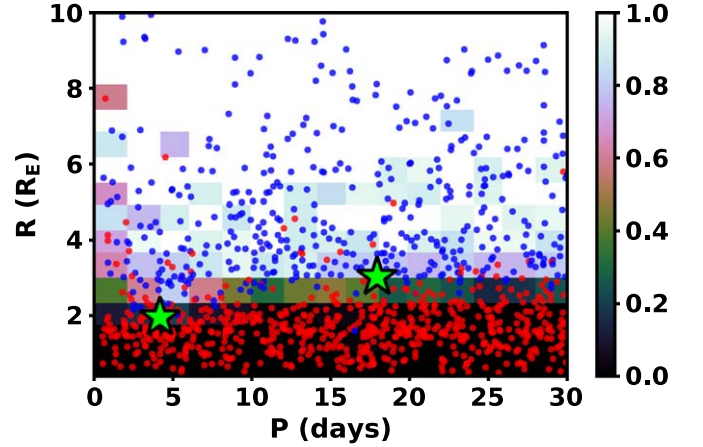
Figure 15. Injection/recovery test for TOI-1224. Each point represents an injected planet, with red points indicating an injected planet we failed to recover, while blue points are ones we recovered successfully. Only 20% of the injected planets are shown for clarity. The background is color-coded by the overall completeness in a given bin. Interestingly, the completeness right around the inner planet is only $\simeq$20%.

We initially fit both planets using `MISTTBORN` but found that planet c undergoes TTVs. `MISTTBORN` is not set up for TTVs, so we opted to run the c planet using the Joint Analysis of Exoplanetary Transits & RVs (`juliet`; Espinoza et al. 2019; see Section 6.3). We also tested running planet b with `juliet` for TTVs as a check and found that the results were consistent and no significant TTV was detected.

We fit 14 parameters in total. The first four were the regular transit parameters: time of inferior conjunction (T_0), orbital

period of the planet (P), planet-to-star radius ratio ($R_p/R_\star$), and impact parameter (b). The fifth parameter was stellar density ($\rho_\star$). Eccentricity was assumed to be zero, but we test this assumption by comparing the density from Section 5 to that from the transit (Figure 10).

For the limb-darkening relation, we assumed quadratic (q_1, q_2) following the triangular sampling prescription of Kipping (2013). We included data from three unique bands, TESS, g_p', and z_s, requiring six limb-darkening parameters in total (see Table 6).

To model stellar variations, `MISTTBORN` includes a GP regression module utilizing the `celerite` code (Foreman-Mackey et al. 2017a). We initially used a mixture of two stochastically driven damped simple harmonic oscillators (SHOs) at the primary period (P_{GP}) and secondary period ($0.5P_{GP}$). However, our analysis revealed that the second SHO was not necessary, prompting us to rerun the model with a

Table 8
Prior and Posterior Distributions for TTV Extraction Using `juliet` for TOI-1224 c

Description	Parameter	Prior[a]	Posterior	$O - C$ (minute)
		TESS TTV Fitting		
Limb darkening	q_1	$\mathcal{U}$ (0.0, 1.0)	$0.61^{+0.24}_{-0.25}$	$\cdots$
Limb darkening	q_2	$\mathcal{U}$ (0.0, 1.0)	$0.14^{+0.18}_{-0.10}$	$\cdots$
Offset relative flux	m_{flux}	$\mathcal{N}$ (0.0, 0.1)	$-0.0001^{+0.0}_{-0.0}$	$\cdots$
Jitter	σ	$\mathcal{J}$ (0.1, 1000.0)	$548.52^{+31.43}_{-32.41}$	$\cdots$
Amplitude of GP	GPσ	$\mathcal{J}$(0.000001, 1000000)	0.0046 ± 0.0001	
Time of GP	GPρ	$\mathcal{J}$ (0.000001, 1000000)	$0.1511^{+0.0036}_{-0.0035}$	
Time of transit center	T_0	$\mathcal{N}$ (2458329.8653, 0.0417)	$2458329.8678^{+0.0015}_{-0.0016}$	$11.56^{+1.83}_{-1.98}$
	T_1	$\mathcal{N}$ (2458347.81055, 0.0417)	$2458347.8105^{+0.0017}_{-0.0017}$	$7.69^{+2.09}_{-2.06}$
	T_{19}	$\mathcal{N}$ (2458670.8250, 0.0417)	$2458670.8174^{+0.0018}_{-0.0017}$	$-8.78^{+2.31}_{-2.21}$
	T_{40}	$\mathcal{N}$ (2459047.6751, 0.0417)	$2459047.6747^{+0.0015}_{-0.0016}$	$-5.23^{+2.18}_{-2.15}$
	T_{41}	$\mathcal{N}$ (2459065.6203, 0.0417)	$2459065.6238^{+0.0016}_{-0.0018}$	$-0.06^{+2.33}_{-2.57}$
	T_{42}	$\mathcal{N}$ (2459083.56560, 0.0417)	$2459083.5636^{+0.0014}_{-0.0016}$	$-8.27^{+2.08}_{-2.21}$
	T_{58}	$\mathcal{N}$ (2459370.6895, 0.0417)	$2459370.689^{+0.0012}_{-0.0013}$	$-11.08^{+1.78}_{-1.88}$
	T_{59}	$\mathcal{N}$ (2459388.6348, 0.0417)	$2459388.6381^{+0.0016}_{-0.0018}$	$-5.9^{+2.27}_{-2.47}$
	T_{99}	$\mathcal{N}$ (2460106.4446, 0.0417)	$2460106.4638^{+0.0011}_{-0.0011}$	$4.33^{+1.77}_{-1.81}$
	T_{101}	$\mathcal{N}$ (2460142.3350, 0.0417)	$2460142.3539^{+0.0012}_{-0.0013}$	$3.12^{+1.83}_{-1.87}$
	T_{102}	$\mathcal{N}$ (2460160.2803, 0.0417)	$2460160.296^{+0.0014}_{-0.0015}$	$-1.70^{+2.09}_{-2.23}$
	T_{103}	$\mathcal{N}$ (2460178.2255, 0.0417)	$2460178.2388^{+0.0013}_{-0.0014}$	$-5.62^{+1.98}_{-1.93}$
		ASTEP TTV Fitting		
Limb darkening	q_1	$\mathcal{U}$ (0.0, 1.0)	$0.31^{+0.31}_{-0.21}$	
Limb darkening	q_2	$\mathcal{U}$ (0.0, 1.0)	$0.41^{+0.33}_{-0.27}$	
Offset relative flux	m_{flux}	$\mathcal{N}$ (0.0, 0.1)	$0.0005^{+0.0002}_{-0.0002}$	
Jitter	σ	$\mathcal{J}$ (0.1, 1000.0)	$4.81^{+98.60}_{-4.46}$	
Time of transit center	T_{80}	$\mathcal{N}$ (2459765.4849, 0.0417)	$2459765.5033^{+0.0033}_{-0.0041}$	$9.03^{+4.61}_{-5.61}$
	T_{81}	$\mathcal{N}$ (2459783.4301, 0.0417)	$2459783.4396^{+0.0021}_{-0.0022}$	$-4.15^{+2.98}_{-3.05}$
		LCO z_s TTV Fitting		
Limb darkening	q_1	$\mathcal{U}$ (0.0, 1.0)	$0.04^{+0.07}_{-0.03}$	
Limb darkening	q_2	$\mathcal{U}$ (0.0, 1.0)	$0.32^{+0.35}_{-0.24}$	
Offset relative flux	m_{flux}	$\mathcal{N}$ (0.0, 0.1)	$0.0003^{+0.0001}_{-0.0001}$	
Jitter	σ	$\mathcal{J}$ (0.1, 1000.0)	$931.92^{+48.13}_{-76.50}$	
Time of transit center	T_{85}	$\mathcal{N}$ (2459855.2111, 0.0417)	$2459855.2278^{+0.0009}_{-0.0009}$	$5.0^{+1.49}_{-1.45}$
		LCO g_p TTV Fitting		
Limb darkening	q_1	$\mathcal{U}$ (0.0, 1.0)	$0.27^{+0.29}_{-0.19}$	
Limb darkening	q_2	$\mathcal{U}$ (0.0, 1.0)	$0.46^{+0.33}_{-0.30}$	
Offset relative flux	m_{flux}	$\mathcal{N}$ (0.0, 0.1)	$0.0005^{+0.0003}_{-0.0003}$	
Jitter	σ	$\mathcal{J}$ (0.1, 1000.0)	$11.18^{+136.10}_{-10.60}$	
Time of transit center	T_{89}	$\mathcal{N}$ (2459926.9921, 0.0417)	$2459927.0137^{+0.0035}_{-0.0039}$	$10.87^{+4.61}_{-5.0}$
		Derived Parameters		
Planet-to-star radius ratio[b]	R_p/R_*	$\mathcal{U}(0, 1)$	0.065 ± 0.001	
Impact parameter[b]	b	$\mathcal{U}(0, 1)$	$0.487^{+0.065}_{-0.083}$	
Eccentricity	e	Fixed	0	
Argument of periastron (deg)	ω	Fixed	90	
Stellar density	$\rho_\odot$	$\mathcal{N}(4.86, 0.66)$	$4.79^{+0.66}_{-0.60}$	
Planet radius	$R_p(\oplus)$	$\cdots$	2.884 ± 0.098	
Period (days)	P	$\cdots$	$17.945466 \pm +0.000012$	
Transit epoch (BJD$_{TDB}$)	T_0	$\cdots$	$2458329.859704^{+0.000828}_{-0.000822}$	

Notes.
[a] $\mathcal{U}(a, b)$ indicates a uniform distribution between a and b, $\mathcal{N}(a, b)$ indicates a normal distribution with mean a and a standard deviation b, and $\mathcal{J}(a, b)$ indicates a Jeffreys prior or log-uniform distribution between a and b.
[b] The transit depth and impact parameters were fit using r_1 and r_2; the values here were transformed back to the (b, p) plane.

Star Name	Cluster/Association	Age (Myr)	R_* ($R_\odot$)	$T_{\rm eff}$ (K)	Planet Name	R_p ($R_\oplus$)	$T_{\rm eq}$ (K)	Period (days)	References
K2-264	Praesepe	700	0.47	3660	b	2.23	496	5.84	Livingston et al. (2019)
					c	2.67	331	19.66	
K2-136	Hyades	700	0.68	4500	b	1.01	610	7.98	Mayo et al. (2023)
					c	3.00	470	17.31	
					d	1.57	420	25.58	
HD 63433	Ursa Major	414	0.91	5640	b	2.11	968	7.11	Capistrant et al. (2024)
					c	2.52	679	20.54	
					d	1.07	1040	4.209	
TOI-2076	Crius 224	340	0.77	5200	b	2.52	797	10.36	Osborn et al. (2022)
					c	3.50	623	21.02	
					d	3.23	530	35.13	
TOI-1224	MELANGE-5	210	0.44	3326	b	2.10	540	4.18	This work
					c	2.88	332	17.95	
TOI-451	Pisces-Eridanus	120	0.88	5550	b	1.91	1491	1.86	Newton et al. (2021)
					c	3.10	875	9.19	
					d	4.07	722	16.36	
HD 109833	MELANGE-4	27	1.00	5881	b	2.89	811	9.19	Wood et al. (2023)
					c	2.59	757	13.90	
V1298 Tau	Taurus	20	1.33	5050	b	9.53	677	24.14	Feinstein et al. (2022)
					c	5.05	968	8.24	
					d	6.13	845	12.40	
					e	9.94	492	44.17	
AU Mic	Beta Pictoris	18	0.82	3665	b	4.19	593	8.46	Donati et al. (2023)
					c	2.79	454	18.86	

single SHO. The GP model consists of three parameters: the period of the GP ($\ln P_{\rm GP}$), the amplitude of the GP ($\ln{\rm Amp}$), and the decay timescale for the variability (quality factor, $\ln Q$). All the GP parameters were explored in logarithmic space.

We applied Gaussian priors on the limb-darkening coefficients based on the values from the `LDTK` toolkit (Parviainen & Aigrain 2015), with errors accounting for errors in stellar parameters and the difference between models used (which differ by 0.04–0.08). A summary of the priors on limb-darkening coefficients can be seen in Table 6. We also applied a Gaussian prior on the stellar density, based on our stellar parameters in Section 5. All other parameters were sampled uniformly with physically motivated boundaries (e.g., $|b| < 1$, $0 < R_P/R_* < 1$, and $\rho_* > 0$).

We ran the MCMC using 100 walkers for 150,000 steps including a burn-in of 20,000 steps. This run was more than 50 times the autocorrelation time for all parameters, indicating that it was more than sufficient for convergence. All output parameters from the `MISTTBORN` analysis are listed in Table 7, with a subset of the planetary parameter correlations in Figure 9 and a subset of the light curve shown in Figure 11.

6.3. TOI-1224 c Planet Parameters and TTV

To measure the transit parameters and account for TTVs, we used `juliet` on the TESS and ground-based light curves. `juliet` (Espinoza et al. 2019)[41] is a Python transit fitting package that utilizes the Python package `batman`

(Kreidberg 2015) to model the transits, `celerite` (Foreman-Mackey et al. 2017a) to model the stellar variability, and `dynesty` (Speagle 2020; Koposov et al. 2023)[42] to perform nested sampling of the posteriors.

6.3.1. TESS Light Curves

`juliet` can simultaneously model the stellar variability, the transit, and the TTVs. We used the TESS light curves after the removal of flares (Section 2.1). We then used a Matern GP kernel implemented in `celerite` (Foreman-Mackey et al. 2017a) to model the stellar variability. This feature is available in the `juliet` code, placing broad priors on the two GP parameters, the amplitude of the GP ($\sigma_{\rm GP}$), and the length scale of the GP ($\rho_{\rm GP}$). The GP parameters were explored in logarithmic space.

In addition to the GP parameters, there are three required instrumental parameters: $m_{\rm dilution}$ (dilution factor), $m_{\rm flux}$ (offset relative flux), and σ (jitter term to account for additional systematic). Since no external contaminating sources were present, the dilution factor was fixed at 1.

To refine the GP model, we identified and removed ~130 data points corresponding to a flare occurring immediately after the ingress of transit number 99 (T_{99}), which was missed by `stella`. This particular subject falls within the time range of 2460106.345 and 2460106.386 BJD$_{\rm TDB}$ and was impacting the GP.

---

[41] ⓞ https://github.com/nespinoza/juliet/

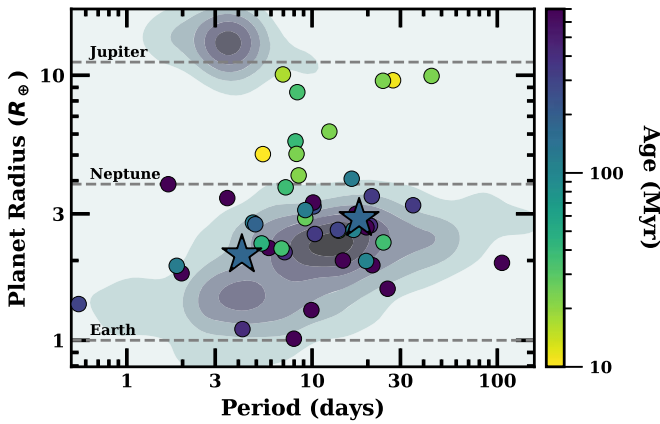[42] ⓞ https://github.com/joshspeagle/dynesty

Figure 16. Contour of all planets discovered by Kepler and K2 as a function of planet radius ($R_{\oplus}$) and orbital period (days). Young (<700 Myr) transiting systems are colored by their approximate age in log space, derived from their respective host cluster or association. TOI-1224 b and c are outlined as stars and fall within the distribution of mature planets. These two planets stand out as rare finds within the age range of ~200 Myr. Planet properties from NASA Exoplanet Science Institute (2020).

6.3.2. Ground-based Data

There were four total TOI-1224 c transits taken with ground-based data: two taken with ASTEP in filter R, one taken by LCO in filter z_s, and another transit taken by LCO in filter g_p (refer to Table 1 for details). All the ground-based data were normalized and detrended. Each data set included the three essential instrumental parameters ($m_{\rm flux}$, $m_{\rm dilution}$, and σ). The dilution factor for each data set was set to 1.

6.3.3. TTV Fitting

Following Espinoza (2018), instead of fitting for the planet-to-star radius ratio ($p = R_p/R_*$) and impact parameter (b), we fit for the parameters for r_1 and r_2. We placed a uniform prior on both these parameters. We adapted a quadratic limb-darkening law, where we placed a uniform prior on both coefficients (q_1 and q_2; Kipping 2013). We set the eccentricity (e) and the argument of periastron (ω) to 0° and 90°. We placed a Gaussian prior on the the stellar density ($\rho_{\odot}$). To model the transit time (T_n), we adopted Gaussian priors with a width of 1 hr for each of the transits. With 16 transits total (12 TESS and 4 ground-based), a dedicated parameter (T_n) was assigned, resulting in a total of 16 T values.

The overall model comprised a total of 35 parameters. The log evidence $\ln(Z)$ for this fit was 6.35 ± 0.19. The transit epoch for planet c is 2458329.8597 ± 0.0008 BJD$_{\rm TDB}$ with a period of 17.945466 ± 0.000012 days. The planet c parameters and resulting observed and calculated time are presented in Table 8. Visualizing the amplitude of the TTVs, Figure 12 offers a graphical representation, while Figure 13 showcases a subset of individual transits. The TTVs of TOI-1224 c deviate from a linear ephemeris by ~10 minutes. With this detection, this system joins the list of young planetary systems exhibiting such phenomena (e.g., TOI-1227; Almenara et al. 2024) and heightens the prospects for further investigation.

6.4. False-positive Analysis

For our false-positive analysis, we first calculate the magnitude limit (Δm) of a potential blended source (bound or background) that could reproduce the transit signal, using
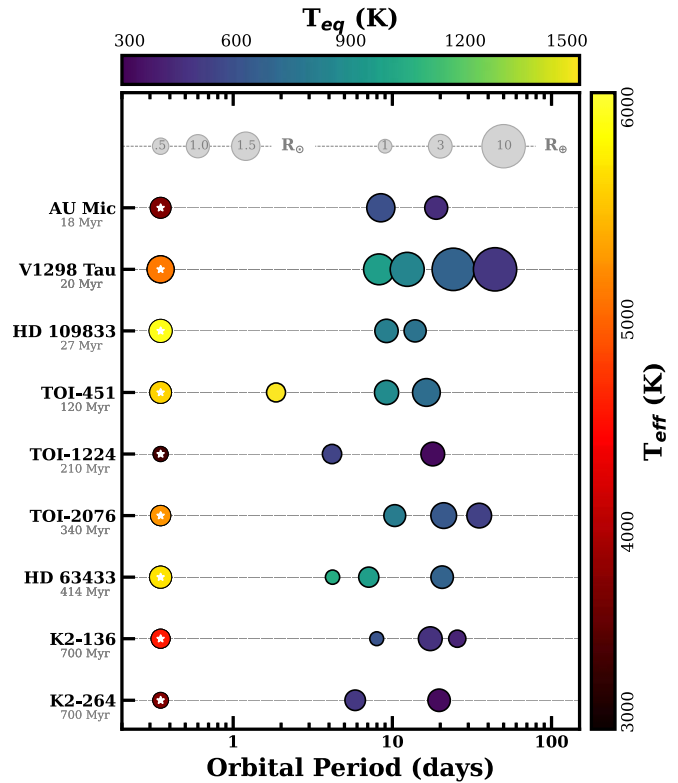
Figure 17. Young (< 1 Gyr), transiting, multiplanetary systems that are members of a known association or a cluster as a function of its period (days). The leftmost circle in each row represents the host star, with the size of the marker proportional to the stellar radius and colored by its effective temperature ($T_{\rm eff}$). The circles to the right represent the planets in each system, with the size of the marker proportional to the planetary radius and colored by its equilibrium temperature ($T_{\rm eq}$). The systems are sorted in order of their age, with the youngest systems at the top and the oldest at the bottom. Data for these planets are listed in Table 9. TOI-1224 follows the intrasystem uniformity pattern (Weiss et al. 2018), as both planets, b and c, share comparable sizes.

the source brightness constraints described by Seager & Mallén-Ornelas (2003) and Vanderburg et al. (2019). This depends on the ingress or egress duration compared to the transit duration and reflects the true radius ratio, independent of whether there is contaminating flux:

$$\Delta m \leqslant 2.5 \log_{10}\left(\frac{T_{12}^2}{T_{13}^2 \delta}\right),$$

where δ is the transit depth, T_{12} is the ingress duration, and T_{13} is the time between the first and third contact. We calculate Δm for the posterior samples for our floating eccentricity transit fit and take the 99.7% confidence limit. We find $\Delta m < 1.3$ and <1.8 for TOI-1224 b and TOI-1224 c, respectively.

Gaia reports a moderately high RUWE (1.475) for TOI-1224. An RUWE above 1.4 is known to be indicative of binarity (Ziegler et al. 2020; Wood et al. 2021). RUWE is known to be higher for young stars (Fitton et al. 2022), but this value is still above most members of the group. TOI-1224 also sits high on the Gaia CMD (Figure 2), although its position is consistent with the intrinsic spread around a single-aged population ($\simeq$0.1 mag based on our isochrone fit; Section 4.1.3). The combination is still suggestive. To be missed in the imaging, spectroscopy, and velocity data, such a companion would need to either be faint or land behind the star

near maximum separation such that most of the velocity is in the plane of the sky. The latter scenario is unlikely but not impossible.

In the case of a bound companion as the source of the transit signals, the resulting signal depth would be a factor of $\simeq 4$ greater for planet b and a factor of $\simeq 6$ greater for planet c. Assuming the companion has the same age, this would still yield a planetary radius for both signals ($\lesssim 7\,R_\oplus$). Although such a scenario would significantly change the inferred radii of the two planets, it does not change the planetary interpretation of the signals and hence rules out any false-positive scenario involving a bound companion.

No Gaia sources within the TESS aperture could reproduce the observed transit shape and depth given the magnitude limits above (Figure 14). The SOAR speckle imaging rules out any such companions down to $\simeq 0.''2$. Lastly, the lack of additional lines in the CHIRON spectra rules out such bright companions assuming they are offset in velocity from TOI-1224 at any of the epochs. This rules out any false-positive scenario involving an unassociated star.

There is also significant separate evidence that the signals are planetary. One is that the transits show consistent depths from g' to z_s (Figure 11). As explained in Désert et al. (2015), if the transit signals were associated with another star in the aperture, the transit depth would vary. The target shows no significant centroid offset (Section 6.1). The transit is consistently detected on the source, including in the (seeing-limited) ground-based photometry. Lastly, the baseline false-positive rate for multiplanet systems is much lower than for targets with a single detected planet (Lissauer et al. 2012, 2014). This has been seen in TESS systems as well (Guerrero et al. 2021). We conclude that both signals are unambiguously planetary in nature.

6.5. Injection/Recovery Analysis

We test our sensitivity to additional planets in the system using an injection/recovery test. For this, we follow Rizzuto et al. (2017). Specifically, we injected 5240 simulated planets with $0.5 < R_P < 10$ and $0.5 < P < 30$. Other parameters, like b and T_0, are drawn from random distributions bounded by physical or data limits. For each simulated planet, we then rerun the `Notch` detection pipeline and attempt to recover the planet. The resulting completeness is shown in Figure 15 and suggests that completeness drops off just below the smaller of the two planets.

7. Summary and Discussion

We report the discovery and validation of two transiting sub-Neptune planets orbiting an early M dwarf, TOI-1224. Stars around TOI-1224 (in space and tangential velocity) have a high fraction of consistent RVs (Figure 2), rapid rotation (Figure 4), high lithium levels (Figure 3), and photometric variability (Section 4.1.4; Barber & Mann 2023), all of which demonstrate that the group is a real young population. Following the convention from prior THYME papers (Tofflemire et al. 2021), we name the group MELANGE-5.

To derive the age of the group, we combine measurements of lithium levels, rotation, and variability resulting in an age of 210 ± 27 Myr. We provide our list of candidate members but with the warning that $\simeq$one-third of the listed targets are likely nonmembers.

MELANGE-5 is physically and kinematically nearby the recently reported groups Crius 224, Theia 424, and Volans-Carina. However, these groups have assigned ages significantly younger than MELANGE-5 (80–110 Myr versus 150–210 Myr). Further investigation is required to establish a more detailed understanding of the relationship (or lack thereof) between these populations. In future work, it would be particularly helpful to model these populations simultaneously to separate out the real membership list.

The youth of TOI-1224 is certain. It exhibits rapid rotation and Hα emission consistent with a <1 Gyr M3V (Kiman et al. 2021). However, the question of whether TOI-1224 is indeed a part of Crius 221, as indicated in Moranta et al. (2022), or MELANGE-5 adds complexity to assigning a precise age. If TOI-1224 is a member of Crius 221, it would account for the slightly elevated position of TOI-1224 in the CMD. If this association holds true and TOI-1224 is a member, it would imply that the star is significantly younger (90–100 Myr). Fortunately, the SED-based R_* works even on pre-main-sequence stars, so the age change would not impact the derived stellar (or planetary) radii, nor would it change the false-positive assessment.

The planets TOI-1224 b and c join the growing number of planetary systems in young associations (e.g., Tofflemire et al. 2019; Newton et al. 2021, 2022). These planets are particularly compelling because there are only a handful of known young multiplanet systems, allowing us to test and refine planetary models within a system. In addition, there are few systems that are within 200–400 Myr, underscoring the significance of TOI-1224 b and c in contributing to our understanding of planetary evolution during this critical epoch.

7.1. TOI-1224 b and c in Context

An increasing number of transiting planets in young associations have been discovered in the last decade (Figure 16), owing mostly to the success of the K2 and TESS missions. The number of such multiplanet systems remains small compared to the older population, in part because K2 and TESS surveyed for a much shorter period than Kepler, and the latter contained only a relatively small number of young stars and stellar associations (e.g., Bouma et al. 2022). We show all known <750 Myr transiting multiplanet systems in known associations in Figure 17. The list grows somewhat if we consider field stars with ages assigned from other methods, such as gyrochronology (Barragán et al. 2022) or lithium (Berger et al. 2018). However, many of these ages are questionable, due in part to the recent discovery of rotation stalling (Curtis et al. 2019a), which has invalidated many earlier age relations for K dwarfs.

Old multiplanet systems are known to show a high level of intrasystem uniformity: masses, radii, and orbital spacings between neighboring planets in compact multiples are more similar than expected by chance (Lissauer et al. 2011; Dawson et al. 2016; Weiss et al. 2018). The current sample of young planets appears to display this trend. However, the sample size of young multiplanet systems is small ($\lesssim 10$). Further, there are various observational biases between the two samples (Rizzuto et al. 2017; Fernandes et al. 2023). Therefore, we regard this as an interesting trend awaiting confirmation through a larger sample of systems and a more comprehensive understanding of these observational biases.

7.2. Prospects for Follow-up

With the launch of JWST, we find ourselves at the forefront of atmospheric characterization in the field of exoplanets. To determine if these planets are suitable targets for observation, we employ the transmission spectroscopy metric (TSM; Kempton et al. 2018). Since these young planets lack directly measured masses, we use the `forecaster` code (Chen & Kipping 2017) to estimate their masses, which assumes these young planets obey the same mass–radius relation as older stars, which may be inaccurate. Given radii of 2.10 and 3.00 $R_\oplus$, the predicted masses using `forecaster` (Chen & Kipping 2017) for TOI-1224 b and c are 5.40 and 8.83 $M_\oplus$, respectively; this resulted in TSM values of 72 and 77. It is important to note that due to their youth, these planets are typically larger and less dense compared to their mature counterparts (Owen 2020). Given that the true masses are likely smaller (as expected for young planets; Owen & Lai 2018; Fernandes et al. 2022), we reevaluated the TSM values with a 30% reduction in radius, resulting in revised mass estimates of 3.03 and 5.03 $M_\oplus$ for planets b and c. Using these values and the actual planet radii leads to an increased TSM value of 128 and 136—making TOI-1224 b and c promising candidates for atmospheric characterization (see also Kempton et al. 2018; Guillot et al. 2022).

While these planets orbit a young host star, obtaining masses for these planets through RV may be challenging, as RV signal from an active star can easily exceed the planetary signal by several orders of magnitude (Tran et al. 2021; Blunt et al. 2023). Nonetheless, the distinctive presence of TTVs in TOI-1224 c provides a promising avenue for future mass constraints. This opportunity is poised to be further explored during the upcoming reobservation of the system in TESS Cycle 7.

ORCID iDs

Pa Chia Thao ⬤ https://orcid.org/0000-0001-5729-6576
Andrew W. Mann ⬤ https://orcid.org/0000-0003-3654-1602
Madyson G. Barber ⬤ https://orcid.org/0000-0002-8399-472X
Adam L. Kraus ⬤ https://orcid.org/0000-0001-9811-568X
Benjamin M. Tofflemire ⬤ https://orcid.org/0000-0003-2053-0749
Jonathan L. Bush ⬤ https://orcid.org/0000-0002-9446-9250
Mackenna L. Wood ⬤ https://orcid.org/0000-0001-7336-7725
Karen A. Collins ⬤ https://orcid.org/0000-0001-6588-9574
Andrew Vanderburg ⬤ https://orcid.org/0000-0001-7246-5438
Samuel N. Quinn ⬤ https://orcid.org/0000-0002-8964-8377
George Zhou ⬤ https://orcid.org/0000-0002-4891-3517
Elisabeth R. Newton ⬤ https://orcid.org/0000-0003-4150-841X
Carl Ziegler ⬤ https://orcid.org/0000-0002-0619-7639
Nicholas Law ⬤ https://orcid.org/0000-0001-9380-6457
Khalid Barkaoui ⬤ https://orcid.org/0000-0003-1464-9276
Francisco J. Pozuelos ⬤ https://orcid.org/0000-0003-1572-7707
Mathilde Timmermans ⬤ https://orcid.org/0009-0008-2214-5039
Michaël Gillon ⬤ https://orcid.org/0000-0003-1462-7739
Emmanuël Jehin ⬤ https://orcid.org/0000-0001-8923-488X
Richard P. Schwarz ⬤ https://orcid.org/0000-0001-8227-1020
Tianjun Gan ⬤ https://orcid.org/0000-0002-4503-9705
Avi Shporer ⬤ https://orcid.org/0000-0002-1836-3120
Keith Horne ⬤ https://orcid.org/0000-0003-1728-0304
Ramotholo Sefako ⬤ https://orcid.org/0000-0003-3904-6754
Olga Suarez ⬤ https://orcid.org/0000-0002-3503-3617
Djamel Mekarnia ⬤ https://orcid.org/0000-0001-5000-7292
Tristan Guillot ⬤ https://orcid.org/0000-0002-7188-8428
Lyu Abe ⬤ https://orcid.org/0000-0002-0856-4527
Amaury H. M. J. Triaud ⬤ https://orcid.org/0000-0002-5510-8751
Don J. Radford ⬤ https://orcid.org/0000-0002-3940-2360
Ana Isabel Lopez Murillo ⬤ https://orcid.org/0009-0006-9572-1733
George R. Ricker ⬤ https://orcid.org/0000-0003-2058-6662
Joshua N. Winn ⬤ https://orcid.org/0000-0002-4265-047X
Jon M. Jenkins ⬤ https://orcid.org/0000-0002-4715-9460
Luke G. Bouma ⬤ https://orcid.org/0000-0002-0514-5538
Michael Fausnaugh ⬤ https://orcid.org/0000-0002-9113-7162
Natalia M. Guerrero ⬤ https://orcid.org/0000-0002-5169-9427
Michelle Kunimoto ⬤ https://orcid.org/0000-0001-9269-8060

References

Abe, L., Gonçalves, I., Agabi, A., et al. 2013, A&A, 553, A49
Alexander, C. M. O., Boss, A. P., & Carlson, R. W. 2001, Sci, 293, 64
Allard, F., Homeier, D., Freytag, B., et al. 2013, MSAIS, 24, 128
Aller, A., Lillo-Box, J., Jones, D., Miranda, L. F., & Barceló Forteza, S. 2020, A&A, 635, A128
Almenara, J., Bonfils, X., Guillot, T., et al. 2024, A&A, 683, A96
Astropy Collaboration, Price-Whelan, A. M., Lim, P. L., et al. 2022, ApJ, 935, 167
Astropy Collaboration, Price-Whelan, A. M., Sipőcz, B. M., et al. 2018, AJ, 156, 123
Astropy Collaboration, Robitaille, T. P., Tollerud, E. J., et al. 2013, A&A, 558, A33
Barber, M. G., & Mann, A. W. 2023, ApJ, 953, 127
Barber, M. G., Mann, A. W., Bush, J. L., et al. 2022, AJ, 164, 88
Barragán, O., Armstrong, D. J., Gandolfi, D., et al. 2022, MNRAS, 514, 1606
Berger, T. A., Howard, A. W., & Boesgaard, A. M. 2018, ApJ, 855, 115
Blunt, S., Carvalho, A., David, T. J., et al. 2023, AJ, 166, 62
Booth, R. A., Clarke, C. J., Madhusudhan, N., & Ilee, J. D. 2017, MNRAS, 469, 3994
Booth, R. A., & Ilee, J. D. 2019, MNRAS, 487, 3998
Bouma, L., Kerr, R., Curtis, J., et al. 2022, AJ, 164, 215
Bouma, L. G., Curtis, J. L., Masuda, K., et al. 2022, AJ, 163, 121
Bouma, L. G., Palumbo, E. K., & Hillenbrand, L. A. 2023, ApJL, 947, L3
Boyle, A. W., & Bouma, L. G. 2023, AJ, 166, 14
Bressan, A., Marigo, P., Girardi, L., et al. 2012, MNRAS, 427, 127
Brown, T. M., Baliber, N., Bianco, F. B., et al. 2013, PASP, 125, 1031
Capistrant, B. K., Soares-Furtado, M., Vanderburg, A., et al. 2024, AJ, 167, 54
Castelli, F., & Kurucz, R. L. 2004, in IAU Symp. 210, Modelling of Stellar Atmospheres, ed. N. Piskunov (San Francisco, CA: ASP), A20
Chatterjee, S., Ford, E. B., Matsumura, S., & Rasio, F. A. 2008, ApJ, 686, 580
Chen, J., & Kipping, D. 2017, ApJ, 834, 17
Collins, K. A., Kielkopf, J. F., Stassun, K. G., & Hessman, F. V. 2017, AJ, 153, 77
Curtis, J. L., Agüeros, M. A., Douglas, S. T., & Meibom, S. 2019a, ApJ, 879, 49
Curtis, J. L., Agüeros, M. A., Mamajek, E. E., Wright, J. T., & Cummings, J. D. 2019b, AJ, 158, 77
Curtis, J. L., Agüeros, M. A., Matt, S. P., et al. 2020, ApJ, 904, 140
Curtis, J. L., Vanderburg, A., Torres, G., et al. 2018, AJ, 155, 173
Cutri, R., Skrutskie, M., Van Dyk, S., et al. 2003, The IRSA 2MASS All-Sky Point Source Catalog
David, T. J., Hillenbrand, L. A., Petigura, E. A., et al. 2016, Natur, 534, 658
David, T. J., Petigura, E. A., Luger, R., et al. 2019, ApJL, 885, L12
Dawson, R. I., Lee, E. J., & Chiang, E. 2016, ApJ, 822, 54
Désert, J.-M., Charbonneau, D., Torres, G., et al. 2015, ApJ, 804, 59
Donati, J. F., Cristofari, P. I., Finociety, B., et al. 2023, MNRAS, 525, 455
Douglas, S. T., Curtis, J. L., Agüeros, M. A., et al. 2019, ApJ, 879, 100
Espinoza, N. 2018, Research Notes of the AAS, 2, 209
Espinoza, N., Kossakowski, D., & Brahm, R. 2019, MNRAS, 490, 2262
ExoFOP 2019, Exoplanet Follow-up Observing Program - TESS, IPAC, doi:10.26134/EXOFOP3
Feiden, G. A., & Chaboyer, B. 2012, ApJ, 761, 30
Feinstein, A. D., David, T. J., Montet, B. T., et al. 2022, ApJL, 925, L2
Feinstein, A. D., Montet, B. T., & Ansdell, M. 2020, JOSS, 5, 2347
Fernandes, R. B., Hardegree-Ullman, K. K., Pascucci, I., et al. 2023, AJ, 166, 175
Fernandes, R. B., Mulders, G. D., Pascucci, I., et al. 2022, AJ, 164, 78
Fitton, S., Tofflemire, B. M., & Kraus, A. L. 2022, RNAAS, 6, 18
Foreman-Mackey, D. 2016, JOSS, 1, 24
Foreman-Mackey, D., Agol, E., Ambikasaran, S., & Angus, R. 2017a, AJ, 154, 220
Foreman-Mackey, D., Hogg, D. W., Lang, D., & Goodman, J. 2013, PASP, 125, 306
Fritzewski, D. J., Barnes, S. A., James, D. J., & Strassmeier, K. G. 2021, A&A, 652, A60
Fritzewski, D. J., Barnes, S. A., James, D. J., et al. 2019, A&A, 622, A110
Gagné, J., & Faherty, J. K. 2018, ApJ, 862, 138
Gaidos, E., Mann, A. W., Lépine, S., et al. 2014, MNRAS, 443, 2561
Galindo-Guil, F. J., Barrado, D., Bouy, H., et al. 2022, A&A, 664, A70
Garcia, L. J., Timmermans, M., Pozuelos, F. J., et al. 2022, MNRAS, 509, 4817
Gillen, E., Briegal, J. T., Hodgkin, S. T., et al. 2020, MNRAS, 492, 1008
Gillon, M., Jehin, E., Magain, P., et al. 2011, EPJ Web of Conf., 11, 06002
Guerrero, N. M., Seager, S., Huang, C. X., et al. 2021, ApJS, 254, 39
Guillot, T., Abe, L., Agabi, A., et al. 2015, AN, 336, 638
Guillot, T., Fletcher, L. N., Helled, R., et al. 2022, arXiv:2205.04100
Günther, M. N., Zhan, Z., Seager, S., et al. 2020, AJ, 159, 60
Harris, C. R., Millman, K. J., van der Walt, S. J., et al. 2020, Natur, 585, 357
Hattori, S., Foreman-Mackey, D., Hogg, D. W., et al. 2021, AJ, 163, 284
Hedges, C., Hughes, A., Zhou, G., et al. 2021, AJ, 162, 54
Hogg, D. W., Bovy, J., & Lang, D. 2010, arXiv:1008.4686
Horne, J. H., & Baliunas, S. L. 1986, ApJ, 302, 757
Howard, W. S., Corbett, H., Law, N. M., et al. 2019, ApJ, 881, 9
Huber, D., White, T. R., Metcalfe, T. S., et al. 2022, AJ, 163, 79
Hunt, Emily L., & Reffert, Sabine 2023, A&A, 673, A114
Hunter, J. D. 2007, CSE, 9, 90
Husser, T.-O., Wende-von Berg, S., Dreizler, S., et al. 2013, A&A, 553, A6
Iyer, A. R., Line, M. R., Muirhead, P. S., Fortney, J. J., & Gharib-Nezhad, E. 2023, ApJ, 944, 41
Jackson, R. J., Jeffries, R. D., Wright, N. J., et al. 2022, MNRAS, 509, 1664

Jeffries, R. D., Jackson, R. J., Wright, N. J., et al. 2023, MNRAS, 523, 802
Jehin, E., Gillon, M., Queloz, D., et al. 2011, Msngr, 145, 2
Jenkins, J. M. 2002, ApJ, 575, 493
Jenkins, J. M., Caldwell, D. A., Chandrasekaran, H., et al. 2010, ApJL, 713, L120
Jenkins, J. M., Tenenbaum, P., Seader, S., et al. 2020, Kepler Data Processing Handbook: Transiting Planet Search, Kepler Science Document KSCI-19081-003, NASA
Jenkins, J. M., Twicken, J. D., McCauliff, S., et al. 2016, Proc. SPIE, 9913, 99133E
Jensen, E. 2013, Tapir: A Web Interface for Transit/Eclipse Observability, Astrophysics Source Code Library, ascl:1306.007
Johnson, M. C., Dai, F., Justesen, A. B., et al. 2018, MNRAS, 481, 596
Johnson, M. C., David, T. J., Petigura, E. A., et al. 2022, AJ, 163, 247
Kempton, E. M.-R., Bean, J. L., Louie, D. R., et al. 2018, PASP, 130, 114401
Kiman, R., Faherty, J. K., Cruz, K. L., et al. 2021, AJ, 161, 277
Kipping, D. M. 2013, MNRAS, 435, 2152
Koposov, S., Speagle, J., Barbary, K., et al. 2023, joshspeagle/dynesty: v2.1.0, Zenodo, doi:10.5281/zenodo.7600689
Kounkel, M., Covey, K., & Stassun, K. G. 2020, AJ, 160, 279
Kreidberg, L. 2015, PASP, 127, 1161
Li, J., Tenenbaum, P., Twicken, J. D., et al. 2019, PASP, 131, 024506
Libby-Roberts, J. E., Berta-Thompson, Z. K., Désert, J.-M., et al. 2020, AJ, 159, 57
Lindegren, L., Klioner, S. A., Hernández, J., et al. 2021, A&A, 649, A2
Lissauer, J. J., Marcy, G. W., Bryson, S. T., et al. 2014, ApJ, 784, 44
Lissauer, J. J., Marcy, G. W., Rowe, J. F., et al. 2012, ApJ, 750, 112
Lissauer, J. J., Ragozzine, D., Fabrycky, D. C., et al. 2011, ApJS, 197, 8
Livingston, J. H., Dai, F., Hirano, T., et al. 2019, MNRAS, 484, 8
Malo, L., Artigau, É., Doyon, R., et al. 2014, ApJ, 788, 81
Mann, A. W., Dupuy, T., Kraus, A. L., et al. 2019, ApJ, 871, 63
Mann, A. W., Feiden, G. A., Gaidos, E., Boyajian, T., & von Braun, K. 2015, ApJ, 804, 64
Mann, A. W., Gaidos, E., & Ansdell, M. 2013, ApJ, 779, 188
Mann, A. W., Gaidos, E., Mace, G. N., et al. 2016a, ApJ, 818, 46
Mann, A. W., Gaidos, E., Vanderburg, A., et al. 2017, AJ, 153, 64
Mann, A. W., Newton, E. R., Rizzuto, A. C., et al. 2016b, AJ, 152, 61
Mann, A. W., Wood, M. L., Schmidt, S. P., et al. 2022, AJ, 163, 156
Masuda, K., & Winn, J. N. 2020, AJ, 159, 81
Mayo, A. W., Dressing, C. D., Vanderburg, A., et al. 2023, AJ, 165, 235
Mayor, M., Pepe, F., Queloz, D., et al. 2003, Msngr, 114, 20
McCully, C., Daily, M., Brandt, G. M., et al. 2022, BANZAI-NRES: BANZAI data reduction pipeline for NRES, Astrophysics Source Code Library, ascl:2212.012
McCully, C., Volgenau, N. H., Harbeck, D.-R., et al. 2018, Proc. SPIE, 10707, 107070K
Mékarnia, D., Guillot, T., Rivet, J. P., et al. 2016, MNRAS, 463, 45
Messina, S., Nardiello, D., Desidera, S., et al. 2022, A&A, 657, L3
Moranta, L., Gagné, J., Couture, D., & Faherty, J. K. 2022, ApJ, 939, 94
Morbidelli, A., Lunine, J. I., O'Brien, D. P., Raymond, S. N., & Walsh, K. J. 2012, AREPS, 40, 251
Muirhead, P. S., Dressing, C. D., Mann, A. W., et al. 2018, AJ, 155, 180
NASA Exoplanet Science Institute 2020, Planetary Systems Table, IPAC, doi:10.26133/NEA12
Newton, E. R., Mann, A. W., Kraus, A. L., et al. 2021, AJ, 161, 65
Newton, E. R., Rampalli, R., Kraus, A. L., et al. 2022, AJ, 164, 115
Öberg, K. I., Murray-Clay, R., & Bergin, E. A. 2011, ApJL, 743, L16
Obermeier, C., Henning, T., Schlieder, J. E., et al. 2016, AJ, 152, 223

Oh, S., Price-Whelan, A. M., Hogg, D. W., Morton, T. D., & Spergel, D. N. 2017, AJ, 153, 257
Osborn, H. P., Bonfanti, A., Gandolfi, D., et al. 2022, A&A, 664, A156
Owen, J. E. 2020, MNRAS, 498, 5030
Owen, J. E., & Lai, D. 2018, MNRAS, 479, 5012
Paredes, L. A., Henry, T. J., Quinn, S. N., et al. 2021, AJ, 162, 176
Parviainen, H., & Aigrain, S. 2015, MNRAS, 453, 3821
Pecaut, M. J., & Mamajek, E. E. 2013, ApJS, 208, 9
Press, W. H., & Rybicki, G. B. 1989, ApJ, 338, 277
Rampalli, R., Agüeros, M. A., Curtis, J. L., et al. 2021, ApJ, 921, 167
Randich, S., Gilmore, G., Magrini, L., et al. 2022, A&A, 666, A121
Rebull, L. M., Stauffer, J. R., Bouvier, J., et al. 2016, AJ, 152, 114
Ricker, G. R. 2014, JAVSO, 42, 234
Riello, M., De Angeli, F., Evans, D. W., et al. 2021, A&A, 649, A3
Rizzuto, A. C., Mann, A. W., Vanderburg, A., Kraus, A. L., & Covey, K. R. 2017, AJ, 154, 224
Rizzuto, A. C., Newton, E. R., Mann, A. W., et al. 2020, AJ, 160, 33
Schmider, F.-X., Abe, L., Agabi, A., et al. 2022, Proc. SPIE, 12182, 121822O
Seager, S., & Mallén-Ornelas, G. 2003, ApJ, 585, 1038
Siverd, R. J., Brown, T. M., Barnes, S., et al. 2018, Proc. SPIE, 10702, 107026C
Skrutskie, M. F., Cutri, R. M., Stiening, R., et al. 2006, AJ, 131, 1163
Smith, J. C., Stumpe, M. C., Van Cleve, J. E., et al. 2012, PASP, 124, 1000
Somers, G., & Pinsonneault, M. H. 2015, MNRAS, 449, 4131
Somers, G., & Stassun, K. G. 2017, AJ, 153, 101
Speagle, J. S. 2020, MNRAS, 493, 3132
Stassun, K. G., Oelkers, R. J., Paegert, M., et al. 2019, AJ, 158, 138
Stassun, K. G., Oelkers, R. J., Pepper, J., et al. 2018, AJ, 156, 102
Stumpe, M. C., Smith, J. C., Catanzarite, J. H., et al. 2014, PASP, 126, 100
Stumpe, M. C., Smith, J. C., Van Cleve, J. E., et al. 2012, PASP, 124, 985
Thao, P. C., Mann, A. W., Gao, P., et al. 2023, AJ, 165, 23
Thao, P. C., Mann, A. W., Johnson, M. C., et al. 2020, AJ, 159, 32
Tofflemire, B. M., Mathieu, R. D., & Johns-Krull, C. M. 2019, AJ, 158, 245
Tofflemire, B. M., Rizzuto, A. C., Newton, E. R., et al. 2021, AJ, 161, 171
Tokovinin, A., Fischer, D. A., Bonati, M., et al. 2013, PASP, 125, 1336
Tokovinin, A., Mason, B. D., Hartkopf, W. I., Mendez, R. A., & Horch, E. P. 2018, AJ, 155, 235
Torres, C. A. O., Quast, G. R., da Silva, L., et al. 2006, A&A, 460, 695
Torres, C. A. O., Quast, G. R., Melo, C. H. F., & Sterzik, M. F. 2008, in Handbook of Star Forming Regions: Volume II, The Southern Sky, ed. B. Reipurth, Vol. 5 (San Francisco, CA: ASP), 757
Tran, Q. H., Bowler, B. P., Cochran, W. D., et al. 2021, AJ, 161, 173
Twicken, J. D., Catanzarite, J. H., Clarke, B. D., et al. 2018, PASP, 130, 064502
Twicken, J. D., Clarke, B. D., Bryson, S. T., et al. 2010, Proc. SPIE, 7740, 774023
Van Eylen, V., Albrecht, S., Huang, X., et al. 2019, AJ, 157, 61
Vanderburg, A., Huang, C. X., Rodriguez, J. E., et al. 2019, ApJL, 881, L19
Vanderburg, A., Mann, A. W., Rizzuto, A., et al. 2018, AJ, 156, 46
Vowell, N., Rodriguez, J. E., Quinn, S. N., et al. 2023, AJ, 165, 268
Wang, D., Hogg, D. W., Foreman-Mackey, D., & Schölkopf, B. 2016, PASP, 128, 094503
Weiss, L. M., Marcy, G. W., Petigura, E. A., et al. 2018, AJ, 155, 48
Wood, M. L., Mann, A. W., Barber, M. G., et al. 2023, AJ, 165, 85
Wood, M. L., Mann, A. W., & Kraus, A. L. 2021, AJ, 162, 128
Zhou, G., Winn, J. N., Newton, E. R., et al. 2020, ApJL, 892, L21
Ziegler, C., Tokovinin, A., Briceño, C., et al. 2020, AJ, 159, 19